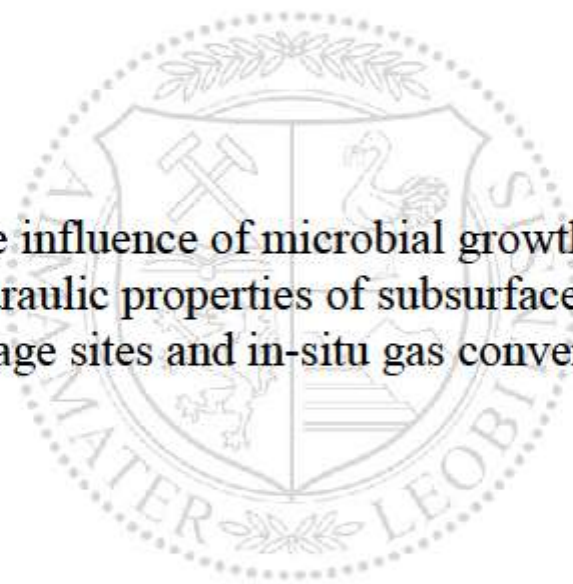




Chair of Reservoir Engineering

Master's Thesis



The influence of microbial growth on
hydraulic properties of subsurface gas
storage sites and in-situ gas conversion

Boris Werner Jammernegg, BSc

September 2020

Boris Werner Jammerneegg

Master Thesis 2020

Supervisors: Univ.-Prof. Dipl.-Phys. Dr.rer.nat. Holger Ott
Dipl.-Ing. Pit Arnold

The influence of microbial growth on hydraulic properties of subsurface gas storage sites and in-situ gas conversion



EIDESSTATTLICHE ERKLÄRUNG

Ich erkläre an Eides statt, dass ich diese Arbeit selbständig verfasst, andere als die angegebenen Quellen und Hilfsmittel nicht benutzt, und mich auch sonst keiner unerlaubten Hilfsmittel bedient habe.

Ich erkläre, dass ich die Richtlinien des Senats der Montanuniversität Leoben zu "Gute wissenschaftliche Praxis" gelesen, verstanden und befolgt habe.

Weiters erkläre ich, dass die elektronische und gedruckte Version der eingereichten wissenschaftlichen Abschlussarbeit formal und inhaltlich identisch sind.

Datum 02.09.2020

A handwritten signature in blue ink, appearing to read 'Boris Werner', written over a horizontal line.

Unterschrift Verfasser/in
Boris Werner, Jammerneegg

Acknowledgements

At the very beginning, I would like to express my endless gratitude to my supervisors Prof. Holger Ott and Dipl.-Ing. Pit Arnold for their excellent guidance, their eminent support, and their trust in me throughout the genesis of my master thesis. I am deeply grateful for the warm reception in your team and the opportunity to conduct scientific research, which led me grow personally as well as professionally.

My sincere thanks to Dr. Neda Hassannayebi, who introduced me to this topic and shared all of her expertise and knowledge with me and immensely supported me especially at the beginning of the model setup and modeling process.

I would also like to express thanks to Dr. Christian Hinz from Math2Market for his support and his expertise for questions related to the simulation software.

I am also thankful to the whole Department of Petroleum Engineering, especially to Ms. Bettina Matzer and Ms. Marlies Helbl for their support and kindness.

Finally, my sincere thanks to my parents, my sister, and my girlfriend for their willingness support and their permanent encouragement, I appreciate that.

Abstract

The global energy market is currently facing a period of transition. To fight the ongoing global warming and to push the decarbonization towards the end of the current century, several countries all over the globe have decided to move from fossil fuels to renewable energy sources in the sector of power generation. The inconstant baseload of those renewable energy sources, such as wind and solar power, created a certain necessity for large-scale energy storage. The idea is to store the power if a surplus is available, and to provide to the grid in case of a lack of energy. Hydrogen gas is an acutely flexible and effective energy carrier, which can be generated via renewable energy in times of surplus. Due to the limited capacity of conventional hydrogen storage techniques, like batteries, depleted gas reservoirs serving as underground hydrogen storage (UHS) are gaining more and more attraction to store large quantities of energy.

This work is based on a doctoral thesis, which was related to UHS in porous media, where a series of experiments were carried out. Among those was an ink-injection experiment, which fueled the suspicion of the presence of a micro-porosity in the accumulated biomass. The experimental results are an integral part of this master thesis.

In this work, the presence of an internal permeability and porosity of accumulated biomass in porous media is studied. Therefore, a numerical model was set up to conduct flow simulations with experimental segmented images with different scenarios and both, uniform and varying permeability as well as porosity cases. Furthermore, the flow field was analyzed in detail. This is the second major topic in this master thesis and is related to the mass transport and nutrient supply within the accumulated biomass. Hence, a python script was written to extract the velocity values between two points of interest within the calculated volume field. To examine whether the supply of nutrients is a result of pure diffusion or rather advection-dominated, the dimensionless Péclet number was calculated in different clusters scattered across the total domain.

This master thesis attempts to contribute to a broader understanding which is relevant for hydrogen storage and conversion operations. The major objective of this research was to survey new concepts via numerical modeling that are significant in the sector of underground energy conversion and storage.

Zusammenfassung

Der globale Energiemarkt befindet sich aktuell in einer Wende. Um die anhaltende globale Erwärmung zu verlangsamen und die Dekarbonisierung bis zum Ende dieses Jahrhunderts voranzutreiben, haben einige Länder dieser Welt beschlossen im Bereich der Stromerzeugung von fossilen Brennstoffen auf erneuerbare Energien umzusteigen. Die inkonstante Grundlast jener erneuerbaren Energie, wie etwa Windkraft und Solarenergie, haben eine gewisse Notwendigkeit für großflächige Energiespeicher kreiert. Die Idee dahinter ist, in Zeiten eines Überschusses den Strom zu speichern, um ihn im Falle eines Mangels wieder ins Netz zu speisen. Wasserstoff ist ein äußerst flexibler und effektiver Energieträger der mittels erneuerbarer Energie, in Zeiten eines Überschusses an Strom, erzeugt werden kann. Da konventionelle Wege der Speicherung von Wasserstoff, wie etwa Batterien, nur begrenzte Speicherkapazitäten aufweisen, gewinnen erschöpfte Erdgaslagerstätten als unterirdische Wasserstoffspeicher (UWS) zunehmend mehr Aufmerksamkeit, um große Mengen an Energie zu speichern.

Diese Arbeit basiert auf einer Dissertation, welche das Thema UWS in porösen Medien behandelte, und im Rahmen derer eine Reihe an praktischen Versuchen durchgeführt wurde. Unter jenen war ein Experiment in der Tinte injiziert wurde, welches den Verdacht nährte, dass die akkumulierte Biomasse eine gewisse Mikroporosität aufweist.

Basierend auf diesen erhaltenen experimentellen Ergebnissen, wurde in der vorliegenden Masterarbeit das Vorhandsein einer internen Permeabilität und Porosität in akkumulierter Biomasse in porösen Medien untersucht. Es wurde ein numerisches Model aufgesetzt um Strömungssimulationen mit experimentell segmentierten Bildern mit unterschiedlichen Szenarien und Fälle mit beidem, einheitlicher und variierender Permeabilität und Porosität durchzuführen. Des Weiteren wurde das Strömungsfeld detailliert analysiert. Dies ist der zweite große Part dieser Diplomarbeit und bezieht sich auf den Stofftransport und die Nährstoffversorgung in der akkumulierten Biomasse. Dazu wurde ein Python-Skript verfasst, um die Geschwindigkeitswerte zwischen zwei Punkten im berechneten Volumenfeld zu extrahieren. Um zu überprüfen ob die Nährstoffversorgung ein Ergebnis reiner Diffusion oder eher advektiv-dominiert ist wurde die dimensionslose Péclet-Zahl für verschiedene Ansammlungen von Biomasse verteilt über die gesamte Domäne berechnet.

Das Ziel dieser Diplomarbeit war zum besseren Verständnis zur Speicherung und Umwandlung von Wasserstoff beizutragen. Das Hauptaugenmerk dieser Arbeit war neue Konzepte mittels numerischer Simulationen, welche von wichtiger Bedeutung für die unterirdische Speicherung und Umwandlung von Energie sind, zu überprüfen.

Table of Contents

Chapter 1.....	23
Introduction.....	23
1.1 Background and Context.....	25
1.2 Scope, Objectives, and Achievements	25
Chapter 2.....	27
Literature Review.....	27
2.1 Biofilms	28
2.2 Microbial Growth, Biofilm Formation, and Clogging	29
2.3 Microbial Transport in Porous Media	30
2.4 Effect on Hydraulic Properties in Porous Media	32
2.5 Effect of Permeable Biofilm	33
Chapter 3.....	39
Numerical Modeling - Pre-processing and Model Setup.....	39
3.1 Experimental Setup – the Basis of Numerical Modeling.....	39
3.2 Image Acquisition and Pre-Processing	41
3.3 Numerical Modeling	43
Chapter 4.....	53
Impact on Hydraulic Properties of Pore-Network	53
4.1 Introduction.....	53
4.2 Permeability and Porosity	54
4.3 Velocity.....	58
4.4 Discussion Section.....	64
Chapter 5.....	67
Summary, Conclusions, and Future Work.....	67
5.1 Future Work.....	69
Chapter 6.....	71
References.....	71
Python Script – Velocity Plot	A-1

List of Figures

Figure 1: Comparison of different hydrogen-based electricity storage options. Hydrogen offers the highest power and discharge duration (Hassannayebi, 2019).	24
Figure 2: Visualization of the life cycle of a biofilm. Bottom left corner – attachment process; bottom center – development and growth of biomass structure; bottom right – fully developed biofilm with detachment of cells; top – developed heterogeneous biofilm. Different gray shades indicate different physiochemical conditions. Additionally, detachment of clusters due to shear forces and formation of streamers at high-velocity areas are shown (Gerlach and Cunningham, 2010).	28
Figure 3: The plot shows the experimental achieved internal and external Pe number versus the biomass accumulation. The external Pe number is always bigger than ten, which indicates advection dominance, as expected in the pore-space, while the internal Pe number crosses the threshold of ten in the course of the simulations for the permeable cases (Pintelon et al., 2012).	35
Figure 4: Shows the internal and external experimental achieved Da number as a function of accumulated biomass. Both definitions of Da number are increasing with time for both, the permeable and impermeable cases, as expected for a system that is increasingly limited in mass transfer (Pintelon et al., 2012).	36
Figure 5: Left - growth velocity potential (after 120 hours), larger in the bottom left corner due to nutrient injection from the left-hand side; right – nutrient concentration (after 360 hours), decreasing nutrient concentration (left to right) as a result of nutrient consumption by bacteria (Landa Marbán et al., 2018).	37
Figure 6: Left - the magnitude of the water flux velocity; right - flow direction of water flux velocity (both after 360 hours); within the biomass a decreasing water flux from the interface to the surface can be noticed. (Landa Marbán et al., 2018)	37
Figure 7: Micromodel chips made from borosilicate glass. The total domain is 1cm x 2cm with channels at the inlet and outlet. The lateral view and the region of interest (ROI) are illustrated (Hassannayebi, 2019).	40
Figure 8: Schematic illustration of the experimental setup. By a syringe pump (A) fluid flow was established and passed the micromodel (B), whereat pressure recording was done by a pressure transmitter (C). Effluent was collected in a beaker (D). Observation via an inverted microscope connected to a processor unit (F). The system was kept in a built-in chamber with heating lines (G), providing constant temperature throughout the experiments (Hassannayebi, 2019).	40
Figure 9: Illustration of the image processing procedure; left – original image, right – final image, simulation input. Images have been converted to 8-bit, the mask of grains was subtracted, finally, the images have been thresholded based on their gray values.	42
Figure 10: Illustration of the image processing procedure. Every single step has been performed with ImageJ/Fiji©.	42
Figure 11: Exemplary comparison of the histograms of the beginning of NF and the end of NF (ROI). The first peak on the right image (Case NF79) belongs to the accumulated biomass. These gray values were subdivided into six groups of biomass with different permeability and porosity.	43
Figure 12: Ink-injection in the micromodel, which affirmed the existence of internal porosity and permeability of the biomass accumulated. (I) Start of ink flooding, (II) ink invasion after 50 minutes: the main pore throats were already filled with ink, whereas other areas are not penetrated yet, (III) invasion of ink after 60 minutes, more regions are affected, (IV) all pores filled with ink after 90 minutes (Hassannayebi, 2019).	46
Figure 13: Comparison of two different timesteps of ROI. Biomass growth in regions which can only be reached by nutrients if the accumulated biomass supplies the mass transport, thus, are not impermeable. These self-contained niches are not directly exposed to fluid flow. The	

nutrient consumption rate must be smaller than the supply to allow growth, which requires an adequate internal permeability of the biomass.	47
Figure 14: Comparison of simulation input at different timesteps to illustrate the variations in permeability and porosity of the biomass. White spots are the grains (quartz), gray is the pore space and the colored accumulations are biomass with different internal permeability and porosity.	48
Figure 15: Illustration of the change in pore space composition. Dark blue colored blocks refer to water, the other blocks represent the biomass with varying permeability and porosity.	48
Figure 16: Simulation input ROI - porosity and permeability values with their corresponding gray values.	49
Figure 17: Illustration of the TD with the exact location of the ROI.....	51
Figure 18: Comparison of the simulation results (ROI). Normalized porosity-permeability reduction for two stages of flooding (BSF and NF). Lower boundary represents the impermeable case (light blue), the upper boundary is the case with an internal permeability of 33.33 D for the biomass (yellow). The fitted dataset (polynomial and power) is the varying permeability case, which shows an evident behavior compared to the cases with uniform permeability.	55
Figure 19: Comparison of experimental and simulation results of the TD. Normalized porosity-permeability reduction for two stages of flooding (BSF and NF). The experimentally obtained data shows a greater reduction in permeability, reasons may be the plugged flowlines and valves, which are not covered in the simulations, and were accompanied by filtration events.	57
Figure 20: Correlation between the growth of biomass and pressure drop across the micromodel over the bacterial suspension flooding (BS flooding) and nutrient flooding (NF). The spikes correspond to filtration events, as indicated in the figure [adapted from (Hassannayebi, 2019)]	58
Figure 21: Velocity count plot of the TD for different internal permeability of the biomass. As expected, the impermeable case achieved the highest velocity values (red line).	59
Figure 22: Flow profile with different internal permeability of the biomass. The spot where the velocity values are taken from is shown on top, the blue line indicates the exact location. Conspicuously is the transition of the profile from the open pore space to the accumulated biomass and vice versa. In the impermeable case, the velocity is zero and is continuously increasing as the internal permeability is raised. This increase in velocity within the biomass is accompanied by a reduction in the overall velocity.....	60
Figure 23: Comparison of the labelled clusters (lower image) at different internal permeability of the biomass (axis of the abscissa). On the ordinate the product of velocity (u) times characteristic length (l) (cluster length) is plotted. D is the diffusion constant, which was set to $1.79e-9$ m ² /s. Based on literature, the transition to the dominance of advection is set to ten. The values must be treated with care, due to the tremendous influence of the characteristic length (l).....	62
Figure 24: Velocity plot over penetration depth (biomass). Velocity at the boundary is a function of the velocity in the pore space and the angle of the accumulated biomass to the velocity vector. The shape of the curve stays always the same, optical variations are due to the lower values achieved with lower internal permeability of the biomass.	63

List of Tables

Table 1: Simulation input - applied boundary conditions for all simulations carried out on the TD and ROI.	51
---	----

Nomenclature

K	permeability	[D]
ϕ	porosity	[-]

Abbreviations

BS	Bacterial suspension
CFT	Colloidal filtration theory
CH ₄	Methane
CO ₂	Carbon dioxide
Da ₁	First Damköhler number
EOR	Enhanced oil recovery
EPS	Extracellular polymeric substances
H ₂	Hydrogen
H ₂ O ₂	Hydrogen peroxide
LB	Lattice Boltzmann
LIR	Left-Identity-Right
MEOR	Microbial enhanced oil recovery
MRT	Multiple relaxation time
NF	Nutrient flooding
Pe number	Péclet number
PtG	Power to Gas
PtX	Power to Energy
REV	Representative elementary volume
ROI	Region of interest
SRT	Single relaxation time
TD	Total domain
UHS	Underground hydrogen storage

Chapter 1

Introduction

The global energy market is currently facing a period of transition. Ambitious goals have been set to fight global warming and to reduce Greenhouse Gas emissions. In recent years, there is a steady trend towards renewable energy sources to reduce the demand of fossil fuels in the sector of power generation. Several energy forecasts claim that the energy demand is continuously increasing towards 2040. It will be a challenging task to provide more energy than today on the one hand and to reduce the carbon dioxide (CO₂) emissions on the other hand. Renewable energies will penetrate the energy market in the upcoming years. A well-known weakness of the most popular renewable energy technologies is the inconstant baseload, which results either in a surplus or a lack of energy they supply to the grid, in contrast to fossil fuels. Thus, energy storage is gaining more and more attention. Hydrogen gas is known as an effective and adaptable energy carrier and has the potential to improve the flexibility of the global energy system. Furthermore, substantial reductions in energy-related CO₂ emissions can be achieved via the generation of hydrogen from renewable energy sources, therefore, contributing to the aspired goal of decreasing Greenhouse Gas emissions. Further, in contrast to the combustion of fossil fuels, hydrogen lowers both, the noise emissions and the local air pollution.

Hydrogen may be an important player in the ongoing decarbonization towards the end of the current century. Smart solutions to store and convert energy in an efficient manner in case of a surplus and to produce energy to impede shortage will be of interest. A recent trend is the utilization and storage of hydrogen or natural gas with an adequate share of hydrogen in porous media in the underground. As a side effect, microbial methanation was observed, which led to the concept of underground energy conversion, where hydrogen and CO₂ are converted via microbial metabolism. In other words, electrical energy is converted into fuel gas by electrolysis, electrical energy is stored via hydrogen. The idea is to inject gaseous hydrogen and CO₂ in a reservoir if a surplus of energy exists which is afterward partially converted to methane

(CH₄). In a period of high energy demand, the CH₄-rich gas mixture is produced and can be transported via the existing gas supply network. The conversion is driven by methanogenic archaea which are part of the aqueous phase located in the subsurface.

In general, the conversion of electricity to a different form of energy carrier or chemicals is achieved via a Power-to-X (PtX) process. Where P represents the surplus of renewable energy and X refers to the transformed energy, like chemicals, gas, hydrogen, or mobility (Hassannayebi, 2019).

Anyhow, geological hydrogen storage requires an adequate geological formation, providing massive storing capacity, such as a depleted gas reservoir, which can be utilized as underground hydrogen storage (UHS) facility. Furthermore, salt caverns are considered as a promising solution, due to their capacity and in-situ conditions to store hydrogen seasonally. Compared to other storage technologies, such as pumped hydroelectricity storage, compressed air energy storage, batteries, and flywheels, geological hydrogen storage features the biggest capacity in power and discharge (see Figure 1). The comparable technologies are limited either in energy density, like batteries or in storage potential and geographical capacity constraints, such as pumped hydro storage. Only a few UHS pilot project have been carried out in the past, thus, there is still a multitude of open questions in terms of feasibility, economic and environmental risk, as the integrity of the eligible formations, possible chemical interactions between the reservoir rocks, the aqueous phase present, and the injected gas (Hassannayebi, 2019; Gabrielli *et al.*, 2020).

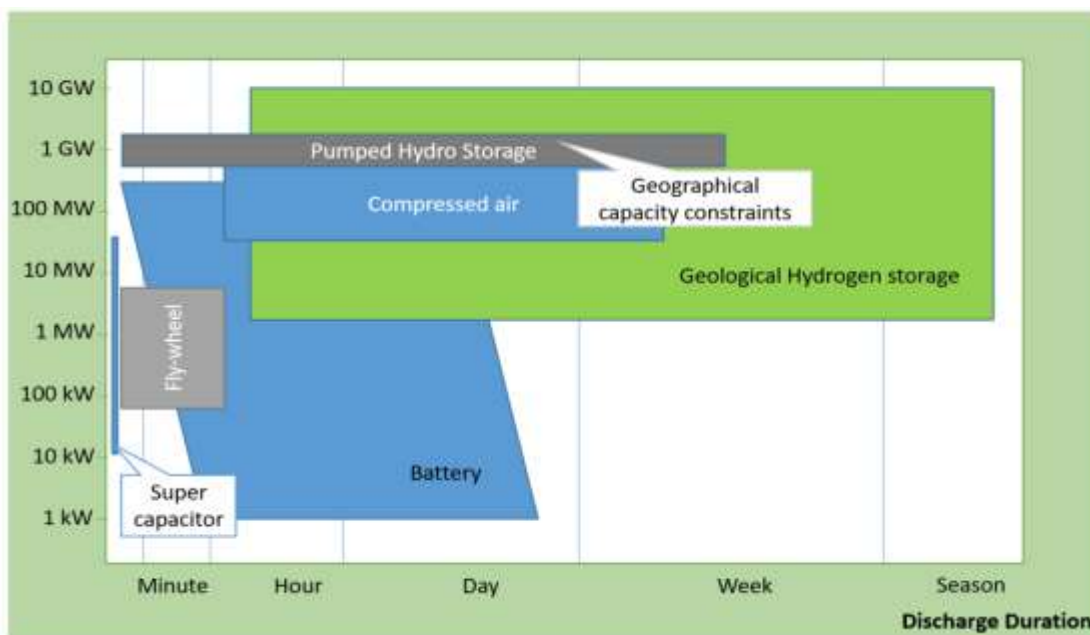


Figure 1: Comparison of different hydrogen-based electricity storage options. Hydrogen offers the highest power and discharge duration (Hassannayebi, 2019).

1.1 Background and Context

This master thesis is based on the dissertation of Dr. Hassannayebi “An assessment of underground hydrogen storage: Transport, geochemistry, and bioactivity”. The doctoral thesis was based on two related projects, “Underground Sun Storage” (www.underground-sun-storage.at), which was related to the storage of large quantities of hydrogen (H_2) in a depleted gas field, and the follow-up project “Underground Sun Conversion” (www.underground-sun-conversion.at), where the focus was put on the production of natural gas-based microbiological processes within a subsurface gas storage.

In the course of the doctoral thesis, experiments were conducted via the usage of micromodel chips. The accumulation of bacteria was captured to quantify the growth of biomass over time. Thereby, an ink-injection test was carried out, which may indicate the presence of an internal permeability and porosity of the biomass. Thus, the experimental achieved time-lapse images have been reused to study this phenomenon and its impact on the hydraulic properties of the pore network in detail. Some papers have been published in recent years which were based on the same assumption. However, they are discussed in detail in the literature review chapter.

To study the behavior of the biomass in detail a numerical model was set up. Different permeability and porosity scenarios and cases were defined and compared. Furthermore, the obtained images were segmented based on their gray values and a varying permeability and porosity case were defined. The goal is, to gain more knowledge about the deviant behavior compared to the case where the biomass is assumed to be impermeable and the mass transport a result of pure diffusion.

To examine whether the supply of nutrients is a result of diffusion or advection, the dimensionless Péclet number (Pe number) was studied in different clusters scattered across the domain.

1.2 Scope, Objectives, and Achievements

The main scope of this master thesis is to study the influence of microbial growth on the hydraulic properties of the pore network. In detail, to study the presence of an internal permeability and porosity of the accumulated biomass within the pore space and its accompanying consequences.

Therefore, a numerical model based on the actual microfluidic model was set up to simulate the biomass with different uniform or varying internal permeability and porosity and to match and compare the results obtained experimentally. Furthermore, the type of mass transfer within the

biomass was studied. The aim is to identify if the mass transfer in the accumulated biomass is a result of diffusion or advection.

The behavior of the biomass at different varying and uniform internal permeability and porosity was studied. A numerical model was developed to analyze the existence of a micro-porosity within the biomass. Several simulations were carried out to study the influence on the hydraulic properties of the pore network. The results indicate that if an internal permeability exists, it is rather minor.

Furthermore, to study the type of mass transport within the biomass, the dimensionless Péclet number was analyzed to determine whether the fluid flow in the biomass is a result of diffusion or advection. The behavior of the velocity at different internal permeability and porosity was studied in detail.

Chapter 2

Literature Review

We are currently facing a period of transition in the global energy market. Ambitious goals were set in recent years, to expand and conquer the renewable energy market. Wind and solar energy play a vital role in the realignment of the energy market and push the energy transition from fossil fuels to renewable energy sources. To provide the same constant baseload to the grid, energy storage is gaining more and more attractiveness, due to the fluctuations in the power supply of wind and solar energy. Therefore, Power to Gas (PtG) technology may build a bridge to manage this issue, via the transformation of renewable energy through electrolysis and methanation of H_2/CO_2 resulting from microbial activity (Götz *et al.*, 2016; Hassannayebi, 2019).

This chapter deals with basic concepts in microbiology. Additionally, clogging types, the microbial transport in porous media, and the impact on the hydraulic properties of the pore network are reviewed.

Microbial interactions, water flow, and solute transport may be linked in porous media and can cause changes in the microbial, chemical, and physical properties over time. As a byproduct, those activities may result in gas production or biomass production and accompanied bioclogging, which refers to the reduction in hydraulic conductivity of a saturated porous media because of the capacity of microorganisms. This may be desirable, to block high permeable regions to avoid bypassing of hydrocarbon in zones of low permeability, such as water flooding of oil and gas reservoirs. Non-desirable bioclogging have been reported from waste disposal operations, and operations where the injectivity of wells was decreased, such as microbial enhanced oil recovery (MEOR) and underground energy storage (Hassannayebi, 2019).

2.1 Biofilms

Microbial biofilms arise in natural as well as in engineered systems - preferentially in aqueous environments - via growth and attachment of microorganisms. During the process of growth, enclosing cells produce extracellular polymeric substances (EPS), to raise the cohesive strength of the biofilm. Furthermore, the EPS matrix acts as a nutrient reservoir. The growth of biofilm in porous media affects the permeability and porosity (bioclogging), and therefore hydrodynamics. Thus, biofilms are processed in enhanced oil recovery (EOR), subsurface remediation, carbon sequestration, hydrogen storage, and many more (Lappin-Scott, Cusack, and Costerton, 1988; Gerlach and Cunningham, 2010).

Gerlach and Cunningham discovered, that three major stages of biofilm development should be considered: first, the microbial transport and attachment, second, the biofilm growth, third, the microbial attachment and propagation (Gerlach and Cunningham, 2010). The following figure illustrates schematically the life cycle of a biofilm: attachment (bottom left), growth and development (bottom center), and entirely developed biofilm (bottom right). At the top of the figure, a fully developed heterogeneous biofilm is shown. Besides that, the detachment of clusters and biofilm streamers are indicated, which can be a result of varying flow conditions due to microbial growth (Gerlach and Cunningham, 2010).

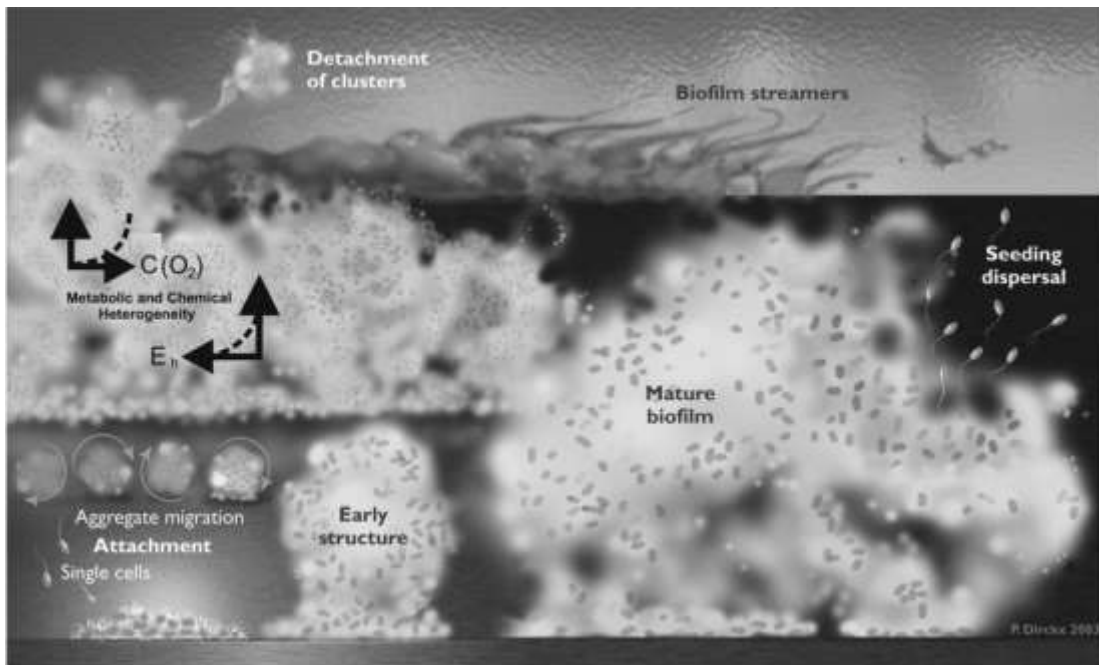


Figure 2: Visualization of the life cycle of a biofilm. Bottom left corner – attachment process; bottom center – development and growth of biomass structure; bottom right – fully developed biofilm with detachment of cells; top – developed heterogeneous biofilm. Different gray shades indicate different physiochemical conditions. Additionally, detachment of clusters due to shear forces and formation of streamers at high-velocity areas are shown (Gerlach and Cunningham, 2010).

Microorganisms are prone to attach to a surface present. Yao et. al state that these mechanisms and kinetics during the process of attachment within porous media are commonly described via the colloid filtration theory (Yao, Habibian and O'Melia, 1971). The withdrawal of nutrients from a flowing fluid is governed by a multiplicity of parameters, such as hydrodynamics, properties of microbial cells, as well as porous media characteristics (Yao, Habibian and O'Melia, 1971; Gerlach and Cunningham, 2010).

2.2 Microbial Growth, Biofilm Formation, and Clogging

A variance of factors is influencing biofilm growth once it is attached to a surface, such as the availability of nutrients, the governing hydrodynamics, and the presence of inhibitors. Gerlach and Cunningham (Gerlach and Cunningham, 2010) predicate five crucial parameters of biofilm formation: (1),(2) sufficient nutrient and energy must be present, (3) adequate geochemical conditions (such as temperature, pH, pressure, etc.), (4) absence of inhibitors (waste products, toxins), and (5) hydrodynamics influencing the solute mass transport (Gerlach and Cunningham, 2010).

Microbial growth is essentially dictated by the availability of nutrients as well as the presence of limiting environmental factors. Liebig's Law of the minimum affirms, if several nutrients are present in comparatively low concentrations, the most growth-limiting substance determines the overall evolutionary population growth. Furthermore, the principle of Shelford's law of tolerance states that there are supplemental factors affecting microorganisms making them not able to grow and survive independently of the nutrient supply, such as a specific temperature window (Warsi and Dykhuizen, 2017; Hassannayebi, 2019).

A biofilm is formed if microbes attach to a surface in a natural environment. Biofilms may form on almost every surface, regardless of completely saturated or undersaturated environments, if sufficient proteins and molecules are present. They may arise in cooling towers, biofilters, pipelines, soils, ship hulls, and a diversity of other environments. A wide difference between biofilms and suspended cells is the usual bulk of EPS present within biofilms. This features biofilms with structural support. Biofilms are set to be a predominant form of microbial life in porous media (Willey *et al.*, 2008; Gerlach and Cunningham, 2010).

Biofilm formation on a surface is a complex phenomenon and consists of a series of events. The characteristics of the solid surface play a vital role throughout the attachment process. The level of microbial colonization raises, as the surface roughness is increased. Donlan (Donlan, 2002) states, that in theory, the flow velocity adjacent to the substratum/fluid interface is negligible. This specific region is the so-called hydrodynamic boundary layer. As the flow velocity is increased, the relative thickness of the hydrodynamic boundary layer decreases.

Another byproduct of higher linear velocity is the employment of higher shear forces – erosion – hence, leading to detachment of cells. Another aspect influencing the rate of microbial attachment are the characteristics of the aqueous medium, such as pH, nutrient concentration, liquid ionic strength, temperature, and many more (Donlan, 2002; Hassannayebi, 2019).

Systems with a large surface area to volume ratio, such as porous media, provide bacteria an appealing habitat. Bioclogging is a major process in the subsurface porous media and its impact on hydraulic properties may be significant. In porous media, Clogging is often referred to as the decline in hydraulic conductivity. It is a reduction in permeability and porosity of porous media, because of the formation of biofilm in pore-spaces (Jeong *et al.*, 2018; Hassannayebi, 2019).

Underground clogging is commonly classified into four subgroups: physical, chemical, and biological clogging. Physical clogging may be a result of clay swelling, migration of fines, accumulation of organic and inorganic suspended solids, or invasion of drilling fluid in porous media. Although clogging is predominantly triggered by physical processes, it is later deteriorated via biological clogging, such as the accumulation of biomass and the growth of biomass. Chemical clogging is referred to precipitations of sulfates, phosphates, calcium carbonates, and other minerals (Martin, 2013; Hassannayebi, 2019).

2.3 Microbial Transport in Porous Media

To model the transport of bacteria in porous media, colloidal filtration theory (CFT) has been widely utilized. One of the crucial factors limiting the transport of bacteria through the pore network is filtration or physical straining of microorganisms via pore throats. Whereas physical straining is a function of the bacterial size and shape (Hassannayebi, 2019).

Bacterial attachment or adsorption can be described via the filtration theory, which is a major control parameter for the movement of bacteria in the pore network. Martin *et. al* (Martin, Bouwer and Hanna, 1992) demonstrated that the application of mechanistic particle transport models to bacteria transport is effective, thus, filtration theory can be used to describe the deposition of bacterial cells in porous media.

2.3.1 Microbial Transport Equations in a Saturated Porous Medium

Tufenkji (Tufenkji, 2007) states, that the temporal and spatial variations of microbe concentration in a homogeneous, saturated porous media are described by the advection-dispersion equation:

$$\frac{\partial C}{\partial t} = D \frac{\partial^2 C}{\partial x^2} - v \frac{\partial C}{\partial x}$$

where C describes the microbe concentration within the aqueous phase at distance x and time t , D represents the dispersion coefficient, and v is the interstitial velocity.

In the equation above, only the processes of physical transport (advection and dispersion) are considered. During the transportation of microbes through a porous media, they are removed from the fluid and attach to the grain surfaces (physicochemical filtration (includes either a reversible or irreversible process)). Independent of the type of the mechanism of attachment used for the description of the removal of microbes from the pore fluid, the governing equations in homogeneous, saturated porous medium becomes (Tufenkji, 2007; Hassannayebi, 2019):

$$\frac{\partial C}{\partial t} + \frac{\rho_b}{\phi} \frac{\partial S}{\partial t} = D \frac{\partial^2 C}{\partial x^2} - v \frac{\partial C}{\partial x}$$

where ρ_b is sediment bulk density, ϕ is the porosity, and S is the microbial concentration attached to the solid phase.

Tufenkji (Tufenkji, 2007) utilized Langmuir and Freundlich isotherms to describe the microbial equilibrium adsorption to the grain surface. If the adsorption is considered to be linear, such as $S = K_{eq}C$, the equation above is written as follows (Tufenkji, 2007):

$$R \frac{\partial C}{\partial t} = D \frac{\partial^2 C}{\partial x^2} - v \frac{\partial C}{\partial x}$$

where R is the so-called retardation factor, $R = 1 + \rho_b K_{eq} / \phi$.

An equilibrium adsorption state is not reached immediately in a suspension of microbes and grains. Two processes control if microorganisms are removed from an aqueous phase, as first-order reactions. First, microbes are transferred from the pore fluid to the grains' surface. Second, the attachment of microbes to the surface because of physicochemical interactions (Tufenkji, 2007).

$$R_A = K_{att}C \qquad R_D = \frac{\rho_b}{\phi} K_{det}S$$

Where R_A and R_D are the rates of attachment/ detachment of microbes to the solid surface, K_{att} and K_{det} represent the rate coefficients of the processes of attachment and detachment. Anyhow, it is worth mentioning that the equations neglect effects like microbial growth (Zhang *et al.*, 2001).

The following one-dimensional equation describes the transport of bacteria, containing terms for storage, reversible as well as irreversible adsorption, advection, and dispersion (Harvey and Garabedian, 1991):

$$\phi \frac{\partial C}{\partial t} + \rho_b \frac{\partial S}{\partial t} = D\phi \frac{\partial^2 C}{\partial x^2} - v\phi \left(\frac{\partial C}{\partial x} + K_{att}C \right).$$

2.3.1.1 Irreversible Attachment

As mentioned, a common approach to evaluate the behavior of microbial transport is the CFT. The irreversible attachment formulation means that the attachment of microbes to grain surfaces is irreversible. This is relevant to the majority of applications that are of practical interest, such as systems that are considered to be steady-state and are primal free of microorganisms, and the effect of dispersion is minor, such as Pe number greater than about 5. At concentration C_0 ($x = 0$) and time t_0 (for continuous particle injection) the equations can be written as follows: (Tufenkji, 2007)

$$C(x) = C_0 \exp\left(-\frac{K_{att}}{v}x\right),$$

$$S(x) = \frac{t_0\phi C_0 K_{att}}{\rho_b} \exp\left(-\frac{K_{att}}{v}x\right).$$

The mass transport process is reflected in η_0 , the single-collector contact efficiency, whereas the step of surface attachment is described via α , the attachment (collision) efficiency. The microbe attachment rate coefficient is related to η_0 and α by (Tufenkji, 2007):

$$K_{att} = \frac{3(1-\phi)v}{2d} \eta_0 \alpha,$$

where d represents the average grain diameter.

2.4 Effect on Hydraulic Properties in Porous Media

The shape and location of accumulated biomass is a function of the hydrodynamic properties in the pore space. Commonly, biofilms adjust their structure over time, thereby optimizing the transport of substrates and their stability. Gerlach and Cunningham (Gerlach and Cunningham, 2010) state, that there can be a tremendous spatial and temporal variability in the accumulation of biofilms, therefore, biofilms do not accumulate homogeneously all-time in porous media. Furthermore, the local hydrodynamics play an essential role. Occasionally, continuous biofilms are formed, but it had been observed, that low permeability areas and flow channels are dominating. Areas that provide certain protections, such as low shear stresses, are preferentially occupied by biofilms, resulting in relatively thick and rough biofilms. In contrast, areas with high shear stress, like pore throats, result, if at all, in thin and smooth layers (Gerlach and Cunningham, 2010).

As a consequence of structural changes, such as changes in permeability and porosity, the pore-scale hydrodynamics are influenced, like the velocity distribution, which affects the intensity of nutrient supply (Carrel *et al.*, 2018).

2.4.1 Porosity

Talking about the porosity of a porous medium affected by biomass, three different types of porosities should be considered: the overall (bulk) porosity and the effective porosity of the porous medium, and the internal porosity of the biomass (Gerlach and Cunningham, 2010). Initially, the internal porosity we thought to be negligible, Thullner and Baveye (Thullner and Baveye, 2008) revealed that and suggested to include an internal porosity and permeability of the biomass in their studies.

The change in porosity is also a function of the pore size distribution in the porous medium itself. Furthermore, the spot of accumulation has also an influence on the degree of permeability reduction. For instance, if biomass is occupying on the inner side of large fractures or pores, even tremendous changes in porosity may not affect the overall permeability. Contrary, the occupation of biomass at locations where their potential to have an effect on the local flow properties is vast, like fracture entrances, or pore throats, also minor changes in porosity may have a major impact on overall or local permeability (Gerlach and Cunningham, 2010).

2.4.2 Permeability

Prevalently, the relative impact due to biomass accumulation in the pore space is expressed via the permeability. Due to the accompanied reduction or even plugging in available pore size, biofilm growth can have an enormous impact on the permeability, so-called bioclogging. Several studies reported a permeability reduction of about three orders of magnitude or less (Gerlach and Cunningham, 2010).

Again, different types of permeability can be distinguished. Not only the permeability of the pore space may be of interest, but also the internal permeability of the biofilm itself, which is discussed in detail on the following pages.

2.5 Effect of Permeable Biofilm

A substantial presumption underlies the most existing biofilm simulation models – the impermeable biomass. In other words, most of the existing models state that the nutrient transport within the biomass is a result of diffusion only. Advective nutrient transport within the biomass is usually neglected. Anyhow, some studies revealed indicators for an internal permeability and porosity within the biomass. Flemming *et al.* (Flemming, Szewzyk and Griebe, 2000) demonstrated, that the morphology of the biofilm is prevalently heterogeneous

and may contain voids. Thus, biofilms are not entirely impermeable. As a result, they may contain a tremendous amount of static as well as dynamic water. Moreover, the total percentage of water in biofilms may be as high as 97% (Flemming, Szewzyk and Griebe, 2000; Pintelon *et al.*, 2012; Ahmad and Husain, 2017).

2.5.1 Modeling Permeable Biofilm

Thullner and Baveye (Thullner and Baveye, 2008) developed a model, where the water in the pore space has a different viscosity as the water within the biofilm. Particularly, the viscosity of the water flowing through the accumulated biomass is given by:

$$\mu_b = X * \mu$$

where μ_b is the viscosity of the biofilm, μ is the actual dynamic viscosity of the fluid, and the parameter X regulates the impact of the biomass on the flow of the fluid in the biofilm. If $X = \infty$, the biofilm acts as impermeable. In contrast, when $X = 1$, the biofilm offers no resistance to flow, thus, acting as a permeable biofilm. In their simulation studies, they used two different values for X to describe the biofilm as impermeable ($X = 10^9$) and permeable ($X = 10^3$) and constant hydraulic head conditions. In contrast to the impermeable biofilm model, the first observation was a remarkable reduction in hydraulic conductivity (two or three orders of magnitude) of the pore networks, which were also observed in laboratory experiments and are in line with observation in field situations (Thullner and Baveye, 2008).

Pintelon *et al.* (Pintelon *et al.*, 2012) suggested utilizing lattice Boltzmann (LB) methods to simulate solute mass transfer and hydrodynamics in a 3D porous media at the pore scale. This method is based on d'Humières *et al.* (D'Humières *et al.*, 2002), who demonstrated that the multiple relaxation time (MRT) LB relaxation rates determine the LB kinematic viscosity, equally as the LB relaxation parameter τ in the single relaxation time (SRT) LB method. The permeability of the biofilm was considered via manipulation of the LB relaxation parameter. The fluid flow was simulated by using MRT LB variant. Therefore, they defined the LB relaxation parameter for flow in simulation lattice nodes which are occupied by biomass, τ_b :

$$\tau_b = n_b * \tau, \quad n_b > 1$$

where n_b describes an impermeability factor of the biofilm. Moreover, they established a proportional relation of n_b and the biofilm apparent viscosity, ν_b . The quotient X of the kinematic viscosities inside the biofilm, the free bulk viscosity, ν , and ν_b . To account for the internal permeability of the region occupied with biofilm, the pseudo-viscosity within the biofilm is set higher ($n_b > 1$) compared to the normal water viscosity. They carried out

simulations for $X = 3, 30, 80,$ and ∞ (impermeable) (D'Humières *et al.*, 2002; Pintelon *et al.*, 2012).

Obviously, their results indicated that via increasing the permeability of the biofilm, an increase in accumulated biomass can be noticed. Further, they obtained higher velocities in the open pore space, as the permeability was reduced. As anticipated, as the permeability is increased, nutrient concentration in the biofilm is larger.

Pintelon *et al.* (Pintelon *et al.*, 2012) carried out a dimensionless number analysis. To quantify the ratio of advective to diffusive mass transfer, the Pe number was utilized:

$$Pe = \frac{u * l}{D}$$

with l as characteristic length and D is the relevant diffusion coefficient. Beyond that, they differed between an internal and external Pe number depending on whether the liquid velocity in the biofilm (u_{bio}), or the bulk liquid velocity (u_{bulk}) is utilized for u . Bijeljic *et al.* (Bijeljic, Muggeridge and Blunt, 2004) proposed that Pe numbers above ten indicate a mass transfer dominated by advection. As illustrated in Figure 3, the external Pe number was permanently in excess of ten, while the internal one experienced a transition from below ten to advection dominated (Bijeljic, Muggeridge and Blunt, 2004; Pintelon *et al.*, 2012).

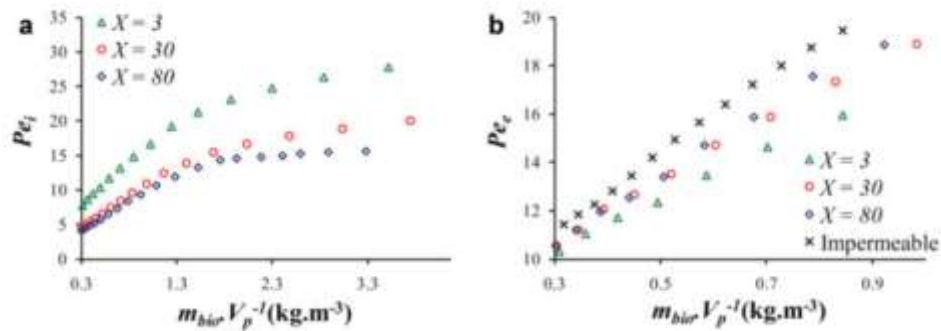


Figure 3: The plot shows the experimental achieved internal and external Pe number versus the biomass accumulation. The external Pe number is always bigger than ten, which indicates advection dominance, as expected in the pore-space, while the internal Pe number crosses the threshold of ten in the course of the simulations for the permeable cases (Pintelon *et al.*, 2012).

Furthermore, the limitation in the mass transfer was investigated. This is best captured via the first Damköhler number (Da_1), which is the ratio of the reaction rate to the advective mass transport rate. Once more, Pintelon *et al.* (Pintelon *et al.*, 2012) distinguished between an internal and an external Da_1 number.

$$Da_I = \frac{q_{max} * \frac{C_N}{C_N + K_N}}{\frac{u}{h}}$$

Where q_{max} is the maximum specific uptake rate, C_N the average nutrient concentration inside the biofilm, and K_N the Monod half-saturation coefficient. Both, the external as well as the internal Da number, were increasing with time as it would be expected for a system that is progressively mass transfer limited (see Figure 4)(Pintelon *et al.*, 2012).

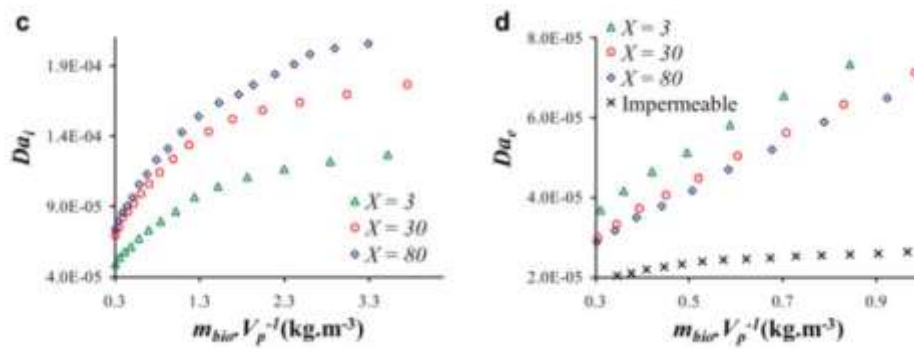


Figure 4: Shows the internal and external experimental achieved Da number as a function of accumulated biomass. Both definitions of Da number are increasing with time for both, the permeable and impermeable cases, as expected for a system that is increasingly limited in mass transfer (Pintelon *et al.*, 2012).

Landa-Marbán *et al.* (Landa Marbán *et al.*, 2018) have built a model for the formation of biofilm including internal porosity and permeability, and have treated the biofilm as a separate phase, like a porous medium itself. Furthermore, the density of the biofilm is not constant:

$$\rho(t, x) = \sum_j \rho_j \theta_j(t, x)$$

where $\rho_j(t, x)$ represents the density, and $\theta_j(t, x)$ is the volume fraction of species j at position x at time t . Note, biomass and water are assumed to be incompressible ($\rho_j = \rho_j(t, x)$). Besides, the water content within the biofilm was assumed to be constant. The flow of water was described via Stokes equations, the water flux inside the biofilm by Brinkman equation. Further, the change in position of the water biomass interface was considered through a varying biofilm thickness (Landa Marbán *et al.*, 2018).

Further, Landa-Marbán *et al.* (Landa Marbán *et al.*, 2018) developed a micro model experiment to match the experimental with the numerical results. A glass micromodel, a camera, and two syringe pumps were utilized to execute the experiments. Microbes and nutrients were injected

for 24 hours in the vertical channel, followed by an entire closure of the vertical channel for one day. Afterwards, nutrients were injected. As illustrated in the following figure, a decreasing nutrient concentration inside the biofilm can be observed from the left to the right, by reason of the nutrient consumption of active bacteria (Landa Marbán *et al.*, 2018).

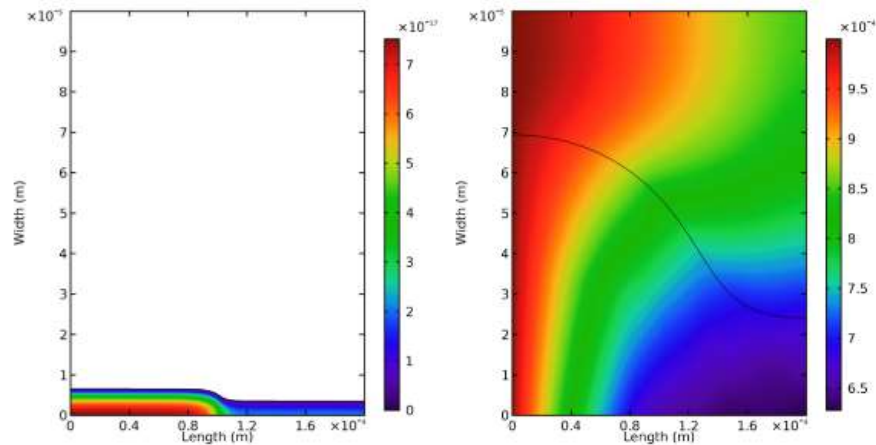


Figure 5: Left - growth velocity potential (after 120 hours), larger in the bottom left corner due to nutrient injection from the left-hand side; right – nutrient concentration (after 360 hours), decreasing nutrient concentration (left to right) as a result of nutrient consumption by bacteria (Landa Marbán *et al.*, 2018).

The following figure shows the flow direction and magnitude of the water flux velocity after 360 hours. It is apparent, that the velocity in the biofilm decreases from the wall to the water-biofilm interface, whereas in the water zone the water flux is larger between the interface and the wall (see Figure 6).

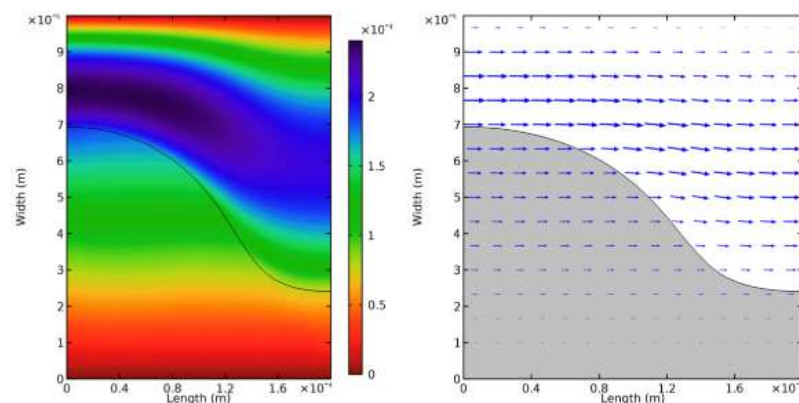


Figure 6: Left - the magnitude of the water flux velocity; right - flow direction of water flux velocity (both after 360 hours); within the biomass a decreasing water flux from the interface to the surface can be noticed. (Landa Marbán *et al.*, 2018)

The numerical simulations delivered a height reduction of biofilm as the water flux velocity was raised. They suggest accounting for the effects of internal flow in the biofilm at higher flow rates, which influences the transport of nutrients and, thus, an influence on the biofilm thickness (Landa Marbán *et al.*, 2018).

Chapter 3

Numerical Modeling - Pre-processing and Model Setup

This chapter deals with the general workflow of the master thesis. In the beginning, the experimental setup of Dr. Hassannayebi is briefly described, for further information and details about the experimental part, please take a look at the doctoral thesis.

Afterward, the focus is put on the numerical model and the general workflow of the thesis. Starting with the image acquisition and pre-processing, where all the major steps of the image processing procedure are described, emphasis is further put on the fundamental equations solved by the simulation software. Moreover, the applied solver, the boundary conditions, as well as the iterative process itself are discussed.

In general, this chapter gives an overview of the work steps conducted throughout the development of the master thesis.

3.1 Experimental Setup – the Basis of Numerical Modeling

In the experiments, the *Lactobacillus Casei* strain was utilized, which is a gram-positive, non-motile rod-shaped, non-spore-forming bacterium, facultatively anaerobic, thus, it can grow in both, aerobic and anaerobic conditions, but it grows faster if oxygen is present. This bacterium has a high resistance and survives in a variety of ambient conditions and can survive in an extended range of pH and temperature. Via the conversion of glucose to lactic acid, the bacterium gets most of its energy (Hassannayebi, 2019).

The experiments were executed via the usage of micromodel chips, which represent a 2D porous media which are made from borosilicate glass (see Figure 7). The depth of the micromodel, permeability, porosity, and pore volume are reported as follows 20 μm , 2.5 D,

0.57, and 4 mm³, respectively. Via wet etching, channels and structures were randomly made. As a result of the etching technique, the lateral view exhibits a curved structure in the depth profile (Hassannayebi, 2019).

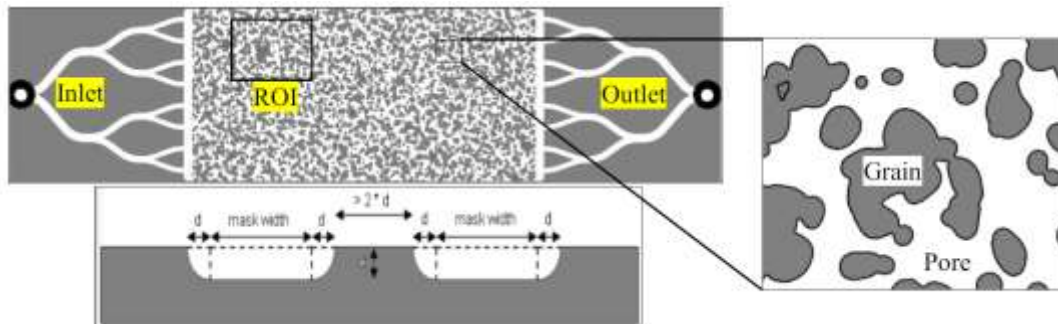


Figure 7: Micromodel chips made from borosilicate glass. The total domain is 1cm x 2cm with channels at the inlet and outlet. The lateral view and the region of interest (ROI) are illustrated (Hassannayebi, 2019).

In Figure 8, the experimental setup is schematically shown. Via time-lapse imaging, the accumulation of bacteria was captured (Hassannayebi, 2019).

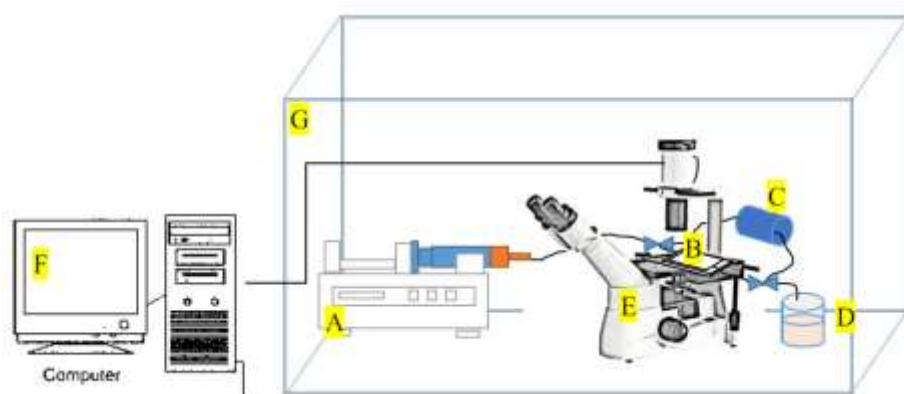


Figure 8: Schematic illustration of the experimental setup. By a syringe pump (A) fluid flow was established and passed the micromodel (B), whereat pressure recording was done by a pressure transmitter (C). Effluent was collected in a beaker (D). Observation via an inverted microscope connected to a processor unit (F). The system was kept in a built-in chamber with heating lines (G), providing constant temperature throughout the experiments (Hassannayebi, 2019).

3.1.1 Experimental Workflow

The experiments were conducted under saturated flow conditions. First, the micromodel was sterilized, then the micromodel was saturated with autoclaved water. Afterward, a single colony-forming unit was inoculated in the fresh medium. Thereafter came phase I, the injection of bacterial suspension (BS flooding), which led to an establishment of biomass, the growth was monitored. Followed by phase II, the injection of nutrients (NF) into the micromodel,

again, further growth of biomass was monitored. Afterward, the micromodel was cleaned via an injection of hydrogen peroxide (H_2O_2) and the usage of an ultrasonic bath (Hassannayebi, 2019).

The duration of the BF flooding was 27 hours, one of the NF was 29 hours. Further details are provided in the work of Dr. Hassannayebi (Hassannayebi, 2019).

3.2 Image Acquisition and Pre-Processing

The utilized images were obtained from experiments conducted in the course of a doctoral thesis, which represents the basis for this master thesis. All image processing steps have been conducted with ImageJ/Fiji®, which is open-source freeware, Java-based image processing program.

At the very beginning, the background of the images was subtracted to correct lens effects (uneven illumination effect). Therefore, the process “Subtract Background” was chosen, the “Rolling Ball Radius” was set 80.0 pixels. Moreover, “Light background” was utilized. This command can be used for the removal of smooth continuous backgrounds from images. The so-called “Rolling Ball Radius” is defined as the radius of the curvature of the paraboloid. Via the application of this algorithm, all peaks which show a larger radius compared to the defined “ball” are subtracted. To allow processing of images which contain dark object and bright background, the “Light Background” option was implemented. As a second step, all images were converted into 8-bit binary images.

Contrary to the impermeable biomass cases, the varying and uniform permeability and porosity cases, the necessity of image enhancement was no more given, to preserve the tiny differences of the gray values within the biomass.

To get information about the narrow difference in gray values of the individual biomass regions, a mask of grains was created to be able to differentiate between those different zones of permeability and porosity within the biomass. Finally, the threshold was adjusted based on their gray values. Therefore, a range of gray values was identified based on the comparison of several histograms of different timesteps (see Figure 11). Furthermore, this range was subdivided into six different regions of permeability and porosity. This was done in a stepwise fashion as illustrated in Figure 16.

In Figure 10 the major image processing steps are illustrated, whereas Figure 9 shows the raw image from the experimental part (left image) and the segmented image (right image), which went through all the listed processing steps.

The above-named processing procedure was applied to the images of the ROI. On the TD no varying permeability and porosity case was set up, thus, the only difference in the image processing procedure is the enhancement of contrast which was applied to the images of the TD.

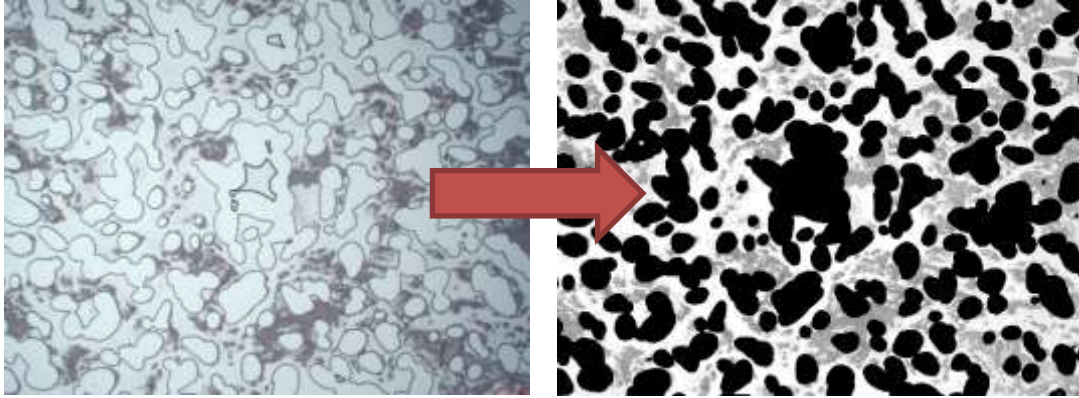


Figure 9: Illustration of the image processing procedure; left – original image, right – final image, simulation input. Images have been converted to 8-bit, the mask of grains was subtracted, finally, the images have been thresholded based on their gray values.

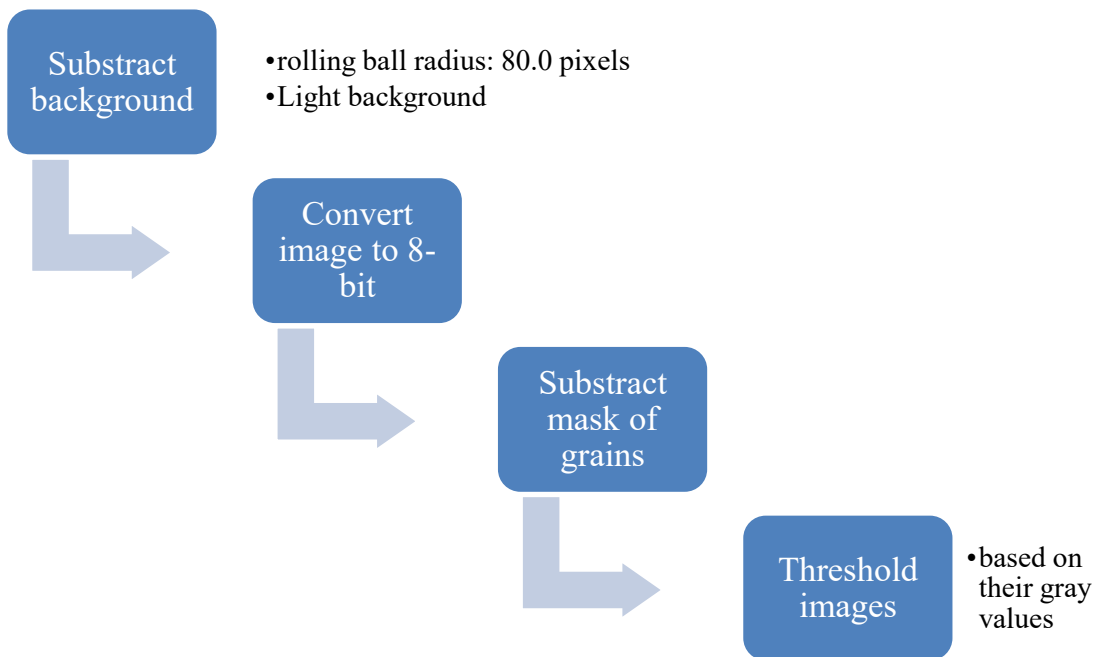


Figure 10: Illustration of the image processing procedure. Every single step has been performed with ImageJ/Fiji©.

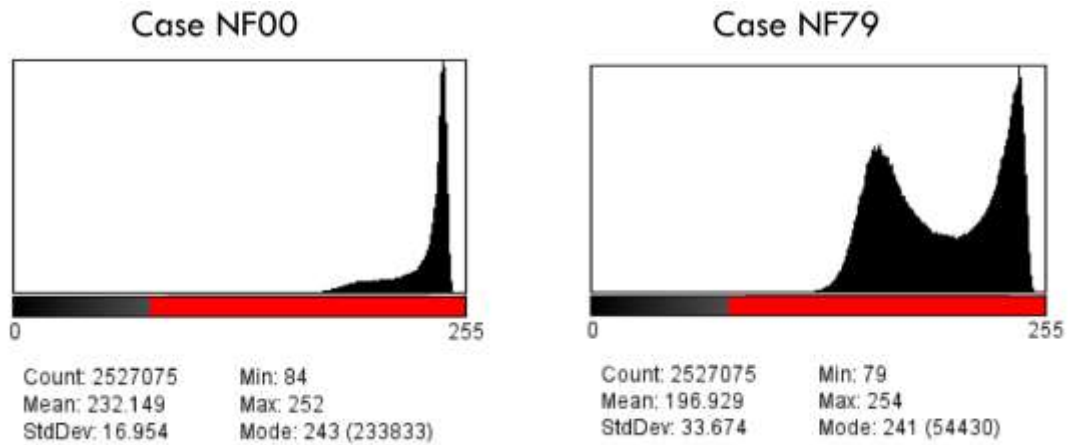


Figure 11: Exemplary comparison of the histograms of the beginning of NF and the end of NF (ROI). The first peak on the right image (Case NF79) belongs to the accumulated biomass. These gray values were subdivided into six groups of biomass with different permeability and porosity.

3.3 Numerical Modeling

The simulations were performed on an 8-core laptop at the very beginning of the work progress, later on, especially for the TD, a 64-core server with 1TB RAM was used.

The GeoDict 2020 Oil and Gas Edition (<https://www.math2market.com>) was utilized for the numerical simulations. The software is capable of importing as well as processing 3D images, building new material structures based on the imported images, analyzing geometries, and predicting certain material properties and behavior and many more.

The computation of the flow field was achieved via the employment of the FlowDict module of the GeoDict software package. This module can compute incompressible, stationary Newtonian flows, where the velocity or pressure tensor is determined iteratively at the voxel scale. By the application of Darcy's law, FlowDict predicts the mean flow velocity for a given pressure drop (experimental pressure drops) which enables the calculation of permeability of a porous structure at the pore scale. Furthermore, the computations of FlowDict assume a steady flow regime, thus time-dependent phenomena, like turbulences, are not considered (Hinz, 2020).

A variety of mathematical equations can be chosen to solve the flow field. The choice is heavily influenced by the structure of the model. If the material consists of empty and solid voxels both, the Stokes equation or the Navier-Stokes equation fit the purpose. If the particle sizes are much smaller compared to the scale of the structure the Brinkman equations (Stokes-Brinkman or Navier-Stokes-Brinkman) are required. The Stokes-Brinkman equation is applied to model linear flows with empty, porous, and solid voxels. It is appropriate to model laminar flow. By

increasing the speed of the flow, a non-linear relationship between mean velocity and pressure drop develops, which can be described via adding the Navier term, thus taking the influence of inertia into account: (Hilden, Linden, and Planas, 2020)

$$-\mu\Delta\vec{u} + (\rho\vec{u} \cdot \nabla)\vec{u} + \nabla p = \vec{f} \quad \text{conservation of momentum}$$

$$\nabla\vec{u} = 0 \quad \text{conservation of mass}$$

where μ is the viscosity of the fluid, ρ is the fluid density, \vec{u} is the velocity of the fluid, p is the pressure, and \vec{f} implies the force density. As mentioned above, via canceling the inertia term $(\rho\vec{u} \cdot \nabla)\vec{u}$, which is part of the Navier-Stokes equation, Stokes equation is obtained and written as follows: (Hilden, Linden, and Planas, 2020)

$$-\mu\Delta\vec{u} + \nabla p = \vec{f} \quad \text{conservation of momentum}$$

$$\nabla\vec{u} = 0 \quad \text{conservation of mass}$$

As discussed before, the additional combination of the existence of a porous medium in a region and a fast fluid flow requires a supplementary set of equations, the Navier-Stokes-Brinkman equations: (Hilden, Linden, and Planas, 2020)

$$-\mu\Delta\vec{u} + (\rho\vec{u} \cdot \nabla)\vec{u} + \mu K^{-1}\vec{u} + \nabla p = \vec{f} \quad \text{conservation of momentum}$$

$$\nabla\vec{u} = 0 \quad \text{conservation of mass}$$

where K^{-1} is the reciprocal of the permeability tensor and μK^{-1} describes the flow resistivity. The complementary term takes porous media that is formed by sub-grid size media into account (Hilden, Linden, and Planas, 2020).

The LIR (Left-Identity-Right) solver was utilized to solve the partial differential equations. This is an appropriate method to model both, linear as well as non-linear fluid flow. The memory requirements of the non-uniform adaptive grids are rather low. Compared to other solvers, the LIR solver is fast for highly porous materials (Linden, Hagen, and Wiegmann, 2014).

The iterative process is regulated by individual simulation stopping criteria, such as error bound, tolerance, maximal iterations, or maximal run time. Moreover, the relaxation factor as well as the grid type and the grid refinement can be adjusted.

Boundary conditions are of paramount importance since they can be pivotal for the resulting quality of the simulations and to ensure a reduction of boundary effects. They dictate the behavior of the fluid in case it is facing an obstacle, or it is in close vicinity to the boundary of

the domain. Different boundary conditions can be applied in the flow direction and the directions tangential to the flow. On the surface of solids, the no-slip boundary condition is used: (Hilden, Linden, and Planas, 2020)

$$\vec{u} = 0.$$

3.3.1 Model Setup

At the very beginning, the simulations of the ROI from the doctoral thesis (Hassannayebi, 2019) have been repeated to get a better understanding and keen sense of the utilized software. An excellent and more detailed description of the experimental setup as well as of the results can be found in the doctoral thesis.

Having conducted all the simulations with the underlying assumption that the biomass is impermeable, the focus was put on the presumption that the biomass has a certain internal porosity as well as permeability. This assumption was proposed in the work of Dr. Hassannayebi, who carried out an ink-injection in the laboratory, which potentially affirmed the existence of internal porosity and permeability of the accumulated biomass, allowing fluid to flow (see Figure 12). The penetration of the ink occurred at a much shorter period than it would be expected for a diffusion dominated process. After approximately 90 minutes of ink injection, all the observed regions were filled with ink (including high dense areas).

Furthermore, regions with no direct contact to fluid flow and therefore, to nutrient supply, grew over time, this may be treated as an indicator for an internal permeability and porosity. Anyhow, if this growth is a result of pure diffusion or advection is not determinable, but it was noticed as a piece of evidence for further studies. In Figure 13, four regions where this phenomenon can be detected are illustrated, three of those are shown in detail. Due to the inaccessibility of the shown spots, the nutrient supply must have happened within the biomass, it is questionable if the transport of nutrient is a result of diffusion or advection. Furthermore, to guarantee growth in these niches, the nutrient consumption rate must be smaller compared to the supply. However, in chapter 4 the dimensionless Pe number was analyzed to study the predominant kind of mass transport within the biomass.

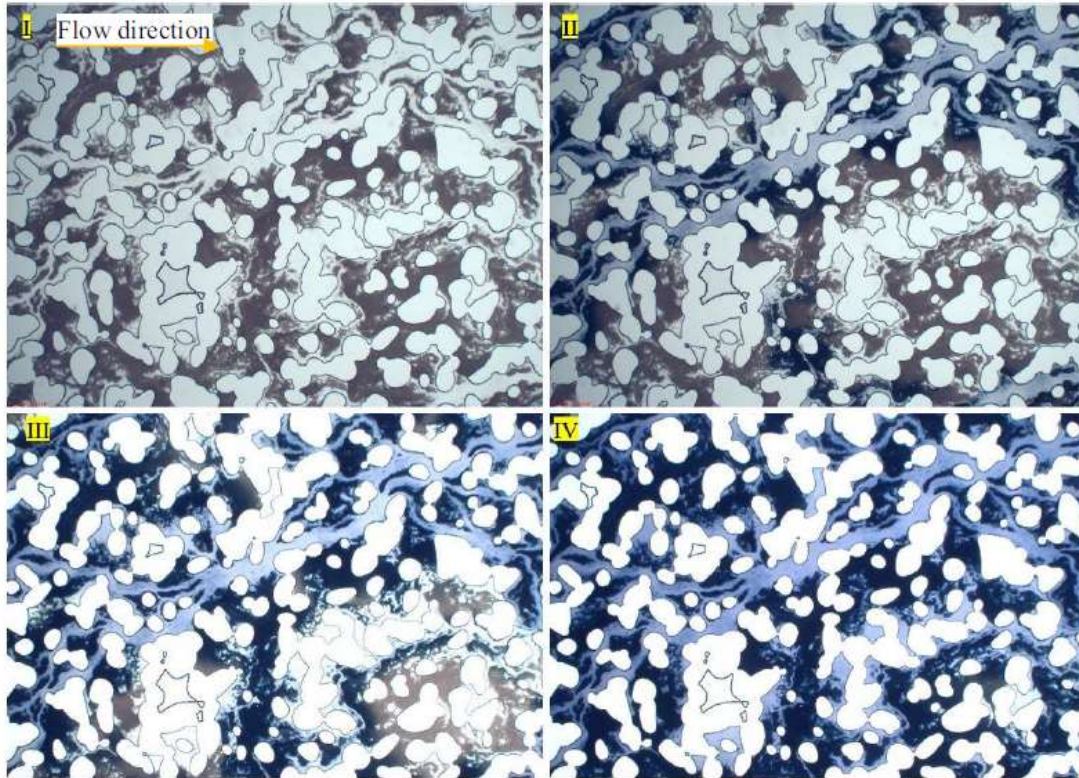


Figure 12: Ink-injection in the micromodel, which affirmed the existence of internal porosity and permeability of the biomass accumulated. (I) Start of ink flooding, (II) ink invasion after 50 minutes: the main pore throats were already filled with ink, whereas other areas are not penetrated yet, (III) invasion of ink after 60 minutes, more regions are affected, (IV) all pores filled with ink after 90 minutes (Hassannayebi, 2019).

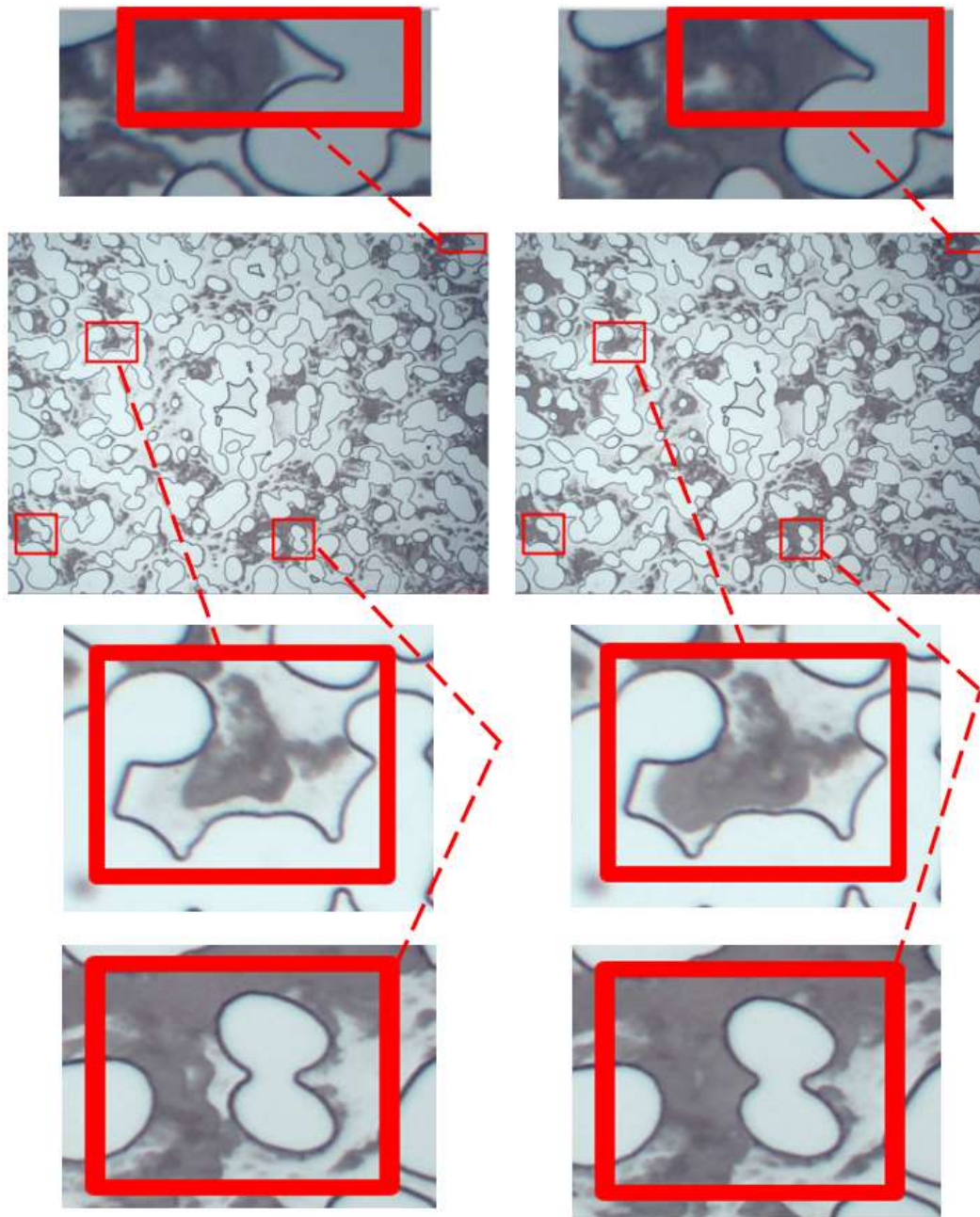


Figure 13: Comparison of two different timesteps of ROI. Biomass growth in regions which can only be reached by nutrients if the accumulated biomass supplies the mass transport, thus, are not impermeable. These self-contained niches are not directly exposed to fluid flow. The nutrient consumption rate must be smaller than the supply to allow growth, which requires an adequate internal permeability of the biomass.

3.3.1.1 Workflow

As a first step, the RAW images were imported into ImageJ/Fiji® to process them as described above. The main difference in the image processing procedure between the impermeable and permeable biomass cases is that the enhancement of the contrast was omitted in the permeable biomass case, to conserve the primordial gray values, which are of paramount importance to distinguish between different zones of permeability and porosity within the biomass (see Figure 14).

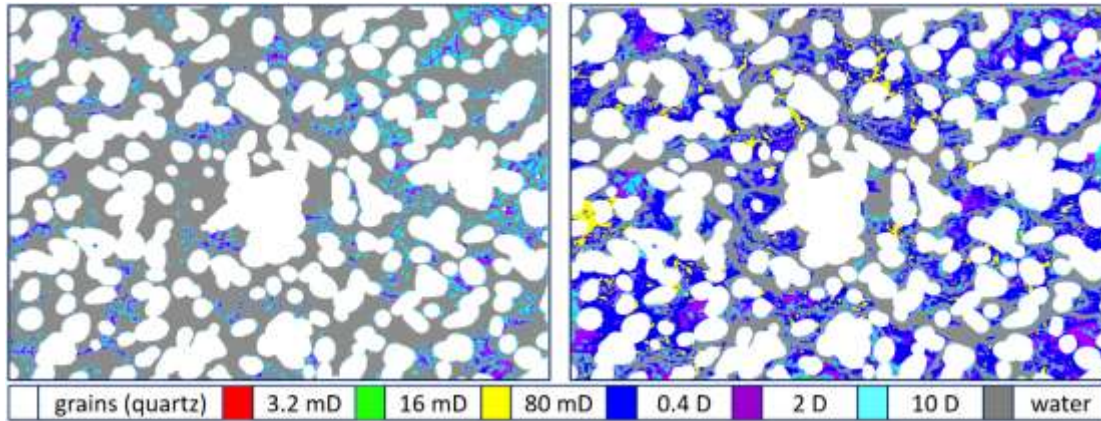


Figure 14: Comparison of simulation input at different timesteps to illustrate the variations in permeability and porosity of the biomass. White spots are the grains (quartz), gray is the pore space and the colored accumulations are biomass with different internal permeability and porosity.

The change in the pore space composition is illustrated in Figure 15. The share of biomass increases by a factor of about 20 over time. The diagram is related to the ROI which explains the massive increase in biomass over time, due to the homogeneous distribution of the biomass. This figure is not valid for the TD.



Figure 15: Illustration of the change in pore space composition. Dark blue colored blocks refer to water, the other blocks represent the biomass with varying permeability and porosity.

As a first guess, the permeability was set between 3.2 mD and 10 D, this follows an exponential trend, whereas the porosity distribution was assumed to follow a linear trend - values between 0.2 and 0.7 were used (Figure 16). Based on the review of Hommel et. al, the relation between the internal permeability and porosity was fitted by the following formula (Hommel, Coltman and Class, 2018):

$$\frac{K}{K_0} \propto \left(\frac{\phi}{\phi_0} \right)^{4.2}$$

where K is the internal permeability of the biomass and ϕ the micro-porosity of the biomass.

In Figure 16, on the axis of abscissa, the six subdomains based on the gray value are illustrated. The grains (quartz) had a gray value of 0, while the pore space corresponds to gray values above 221.5, gray values in the range from 77.5 to 221.5 were assigned to the biomass.

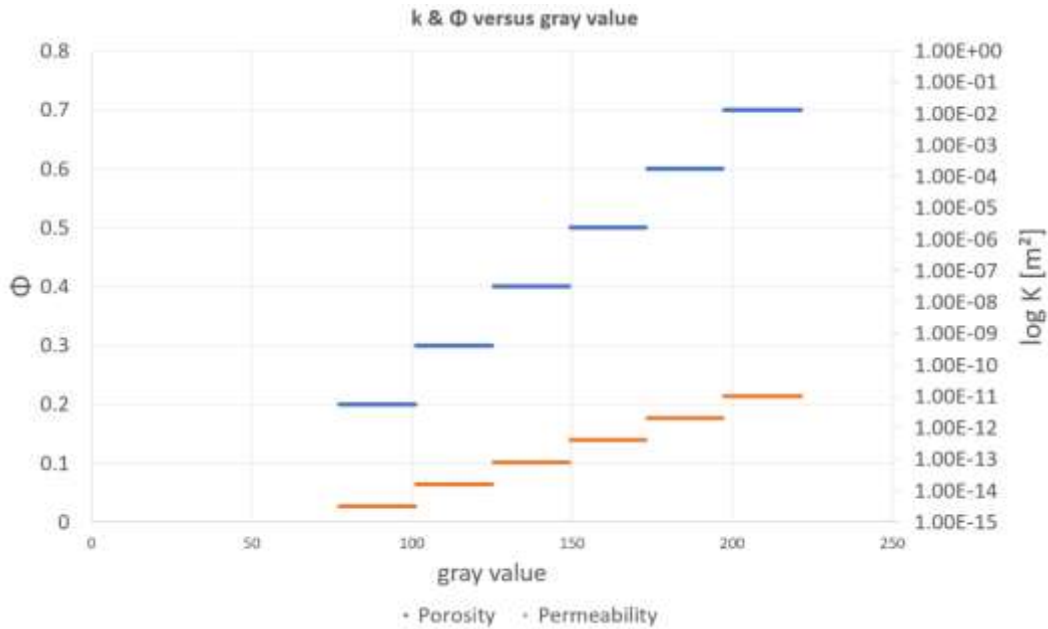


Figure 16: Simulation input ROI - porosity and permeability values with their corresponding gray values.

As a subsequent step, the thresholded images were imported into GeoDict with the ImportGeoVol module. This module allows global thresholding which was utilized to split the gray values which belong to the biomass into six equivalent subregions. Thus, the structure consists of three main groups - the biomass, the grains, and the pore fluid (Figure 14). To transform the image into a three-dimensional structure, the LayerGeo module was used, and four additional layers were added in the z-direction to receive a digital twin of the experiments. This fact implies a certain deviation to the micromodel, which is edged and may contribute to the gap between the experimental and numerical results, which are discussed in detail later in the thesis.

Each layer had a thickness of 1.828 μm , ending up with a total thickness of 9.14 μm , which results in less than half of the thickness of the micromodel (20 μm) utilized in the experimental part of the doctoral thesis. Hence, the empty structure (without biomass accumulation) was simulated with varying depth to match the k_0 of the micromodel, which is set to be about 2.5 D. This value was best fitted with 5 layers, where a permeability of 2.31 D was reached.

Having built the structure, the FlowDict module was utilized in the following steps. To achieve some quick results, the very first simulations were done with Stokes-Brinkman equations on the ROI model, which requires less computational power in contrast to the Navier-Stokes-Brinkman equations. The temperature was set, according to the experimental data, to 37°C, the constituent materials were defined as discussed above. The pressure drop was set constantly at 2000 Pa for the ROI model, since the experimental pressure drop did not correlate to the pressure difference in the sub-domain. In contrast, experimentally measured pressure variations arising from bacterial growth and filtration events were considered in the simulations on the TD model.

All simulations have been executed with the LIR solver, the error bound was set to 0.05 for the flow permeability of the ROI cases, and 0.1 for the TD cases. To lower the computational time, but avoid getting too far off track, the relaxation factor was set to 1.1 for all simulations conducted.

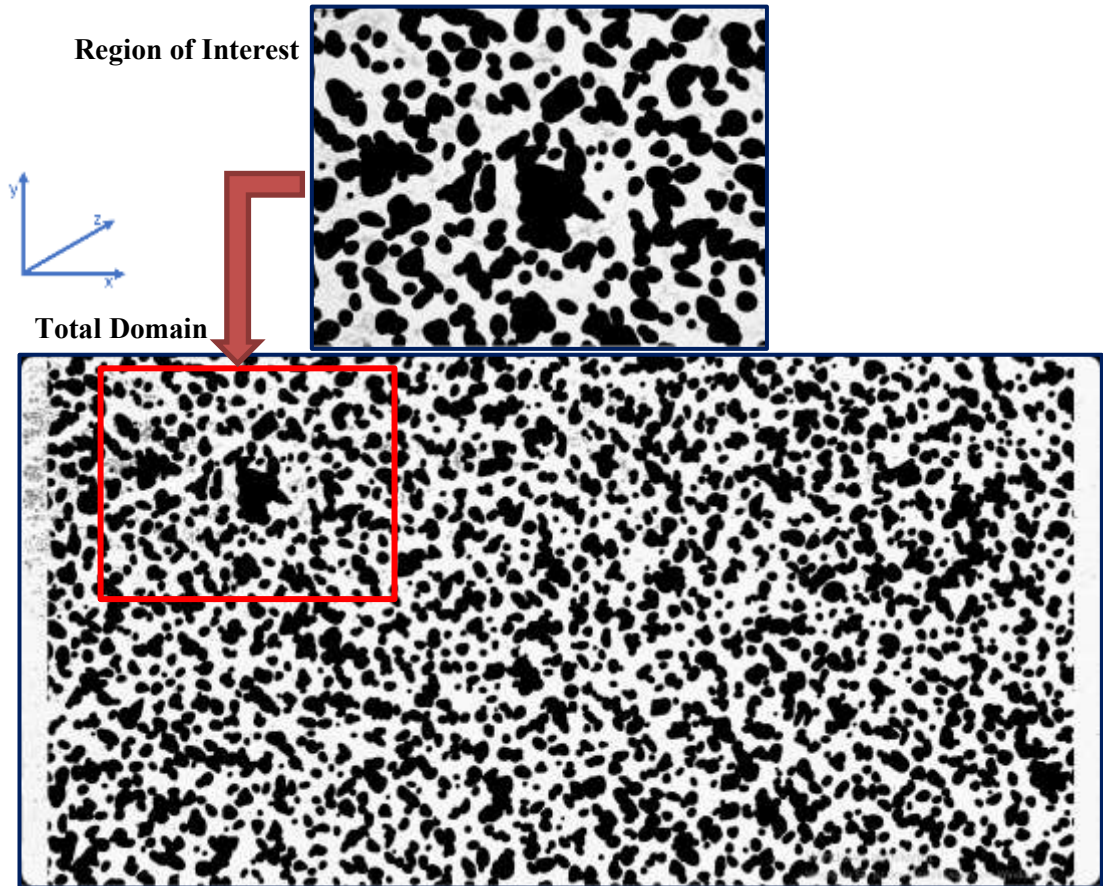


Figure 17: Illustration of the TD with the exact location of the ROI

The figure above displays the location of the ROI within the TD. The boundary conditions in the ROI and TD models were similar, with two major difference, the boundary conditions in the flow direction as well as the pressure drop (compare Table 1). “No-slip” boundary condition, which implies that the fluid velocity at the solid surfaces is defined as zero, was utilized in the z-direction (tangential to flow direction). In flow-direction, the boundary conditions represent the inlet and outlet conditions of the model. The symmetric boundary condition was applied to the ROI model, which connotes a mirroring of the model. Concerning the TD model, periodic boundary condition was used, due to the fact, that the heavy accumulation of biomass in close vicinity to the inlet required an additional implicit in-flow as well as an out-flow region with a size of 10 voxels.

Domain	BCs (x-direction)	BCs (y-direction)	BCs (z-direction)	Pressure Drop
ROI	Symmetric	No-slip	No-slip	Const. = 2000 Pa
TD	Periodic	No-slip	No-slip	experimental pressure drops

Table 1: Simulation input - applied boundary conditions for all simulations carried out on the TD and ROI.

To account for the internal permeability and porosity of the biomass a model with six different zones of permeability and porosity was created. Where the case with impermeable biomass served as a lower boundary, and the case with an internal permeability of 33.33 D represented the upper boundary. Whereat the upper boundary equals to the case of open pore space based on the depth of the micromodel, thus, it is the maximum assignable permeability for the pore space since permeabilities in excess of 33.33 D would lead to an flow enhancement. The upper boundary is based on the Hagen-Poiseuille equation ($W = 20 \mu\text{m}$):

$$\bar{u} = -\frac{W^2}{12\mu} \nabla P$$

Where \bar{u} is the mean velocity, W the thickness in the z-direction, μ the viscosity, and P the pressure. Cases with constant internal permeability of the biomass have been simulated on the TD model. Anyhow, the results, which are discussed in detail in chapter 4, indicated that the internal permeability is far below the upper boundary. Thereby, further simulations were conducted with uniform permeability varying between 1 mD and 500 mD.

Chapter 4

Impact on Hydraulic Properties of Pore-Network

This chapter deals with the impact on the hydraulic properties of the pore space if the biomass has an internal permeability and porosity. Therefore, the individual cases of uniform and varying internal permeability and porosity are compared. This was done for both, the ROI as well as the TD.

Furthermore, the behavior of the flow field at different permeabilities and porosities is studied. At the beginning, the occurrence of arising velocities at different uniform permeabilities was evaluated with the use of a macro. Moreover, to investigate whether the mass transport within the biomass is based on advection or diffusion, the dimensionless Pe number was utilized to compare different cases of biomass permeability and porosity. Farther, the velocity distribution within the biomass was analyzed.

4.1 Introduction

The pore morphology or pore surface network can be altered by several processes coupled to fluid flow and its interactions, such as clay dispersion, sedimentation, and microbiological activities (Ott *et al.*, 2014; Hommel, Coltman, and Class, 2018). Therefore, to gain a thorough knowledge of the morphology alterations, the hydraulic properties of the pore-network can be evaluated. Hence, a permeability-porosity relationship was set up for both models, ROI and TD, to investigate the influence of internal permeability and porosity of the biomass and to compare the individual created cases to each other.

Biomass can show a variety of shapes as it is growing in porous media. Several factors have an impact on the accumulation of biomass, such as the biomass distribution within the pore space,

the biomass structure, the nutrient supply and concentration, environmental conditions, and flow shear stresses.

In general, biomass accumulation decreases permeability and porosity. They may accumulate as stream tracer, especially in high-velocity areas, as biofilms, which equates a thin layer covering the surface of a solid, or as bigger aggregates in the form of clumps.

4.2 Permeability and Porosity

The permeability values were achieved via numerical modeling as described in the previous chapter. In contrast, the porosity was determined by image processing. The normalized porosity-permeability reduction ($1-\phi/\phi_0$ and K/K_0) relationship for two stages of flooding (BS flooding and NF) are displayed in Figure 18 below. As already mentioned, and illustrated in the figure below, the case with impermeable biomass served as a lower boundary, whereas the one with a uniform permeability of 33.33 D served as an upper boundary. In between, three cases with uniform permeability are shown (0.1 D, 1 D, and 10 D). Additionally, the case with varying permeability and porosity is illustrated, which shows a different behavior due to the decrease in permeability and porosity as the accumulated biomass increases. Moreover, this case shows two different trends, the concave part of the curve belongs to the BS flooding, while the convex-shaped part of the curve belongs to NF, which is accompanied by a stronger reduction in porosity and permeability since nutrients are promoting biomass growth. The significant curve progression can be best understood via comparison of Figure 15, which shows the composition of the pore space at different time steps, and Figure 18. In the beginning, the pore space was predominantly occupied with biomass having an internal permeability of 10 D, thus, fitting the uniform (10 D) permeability case. Later, as more and more biomass accumulated in the pore space, the share of 2 D and 0.4 D are significantly increasing. At the end (NF 79) the 0.4 D biomass is dominating, the share of 10 D and 2 D are roughly evenly distributed, the share of 0.08 D is minor. Therefore, the simulated values of the varying permeability and porosity case are located in between the results of the uniform cases of 0.1 D and 1 D (see Figure 18). As mentioned previously, all six subgroups of biomass with different internal permeability and porosity are present, they only differ in their share (see Figure 15).

A best curve fitting approach was implemented, whereat the BS flooding part is fitted by polynomial trend function and the NF part is fitted by a power function (see Figure 18). In contrast to the varying permeability case, the uniform permeability cases can be described with a single power law behavior.

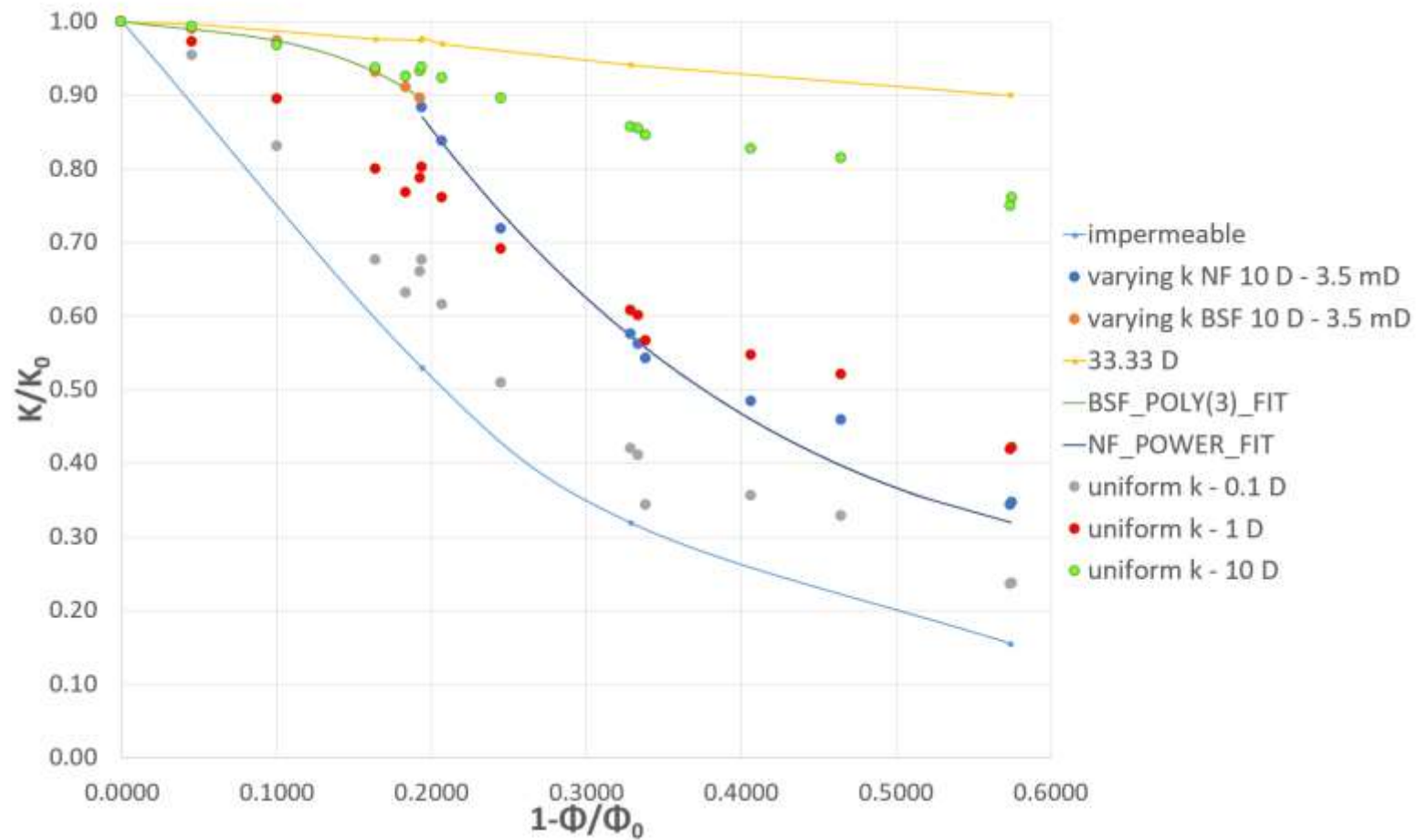


Figure 18: Comparison of the simulation results (ROI). Normalized porosity-permeability reduction for two stages of flooding (BSF and NF). Lower boundary represents the impermeable case (light blue), the upper boundary is the case with an internal permeability of 33.33 D for the biomass (yellow). The fitted dataset (polynomial and power) is the varying permeability case, which shows an evident behavior compared to the cases with uniform permeability.

Both simulated models showed a different relationship between porosity and permeability. The major reason for this inequality is the homogeneous distribution of biomass within the ROI model, due to the close proximity to the inlet, whereas the TD shows a heterogeneous biomass distribution (compare Figure 18 and Figure 19). Another significant impact comes from the filtration events due to sudden release of biomass, which entered the pore space as a so-called cloudy stream, accumulated in the flowlines and valves of the micromodel which are corresponding to the spikes in Figure 20 (Hassannayebi, 2019).

The results of the TD indicate that a distinction between the minor internal permeability cases, such as 1 mD to 100 mD, and the impermeable case is rather difficult due to the marginal differences (see Figure 19). Above 100 mD the results may be distinguished with the naked eye. Again, the high-permeability case, 33.33 D, served as the upper boundary. The gap between the experimentally obtained data points to the simulated ones may be based on filtration effects. The numerical models did not include the inlets and outlets of the micromodel, thus, the effect of the biomass accumulated in the flowlines and valves, which consequently results to an overall increased pressure drop, is not explicitly included in the numerical simulations. At the beginning and after the first filtration event, this gap is getting narrower.

The significant gap between about 0.1 and 0.5 on the axis of abscissa and 0.4 to 0.7 on the ordinate is based on a heavy filtration event that occurred at the beginning of NF, consequently, porosity and permeability are reduced. Whereas the simulated points are closely packed prior to the first filtration event, they are noticeable scattered afterward and show different reductions in permeability as expected. At about 0.5 on the x-axis, the second filtration event happened, again accompanied by a decrease in porosity as well as permeability. Contrary to the ROI model, where two different trends (polynomial and power fit) were detectable in the BS flooding and NF, the TD model did not show such a significant behavior. Reasons may be found in the heterogeneous distribution of biomass in the TD, whereas the ROI showed a rather homogeneous one.

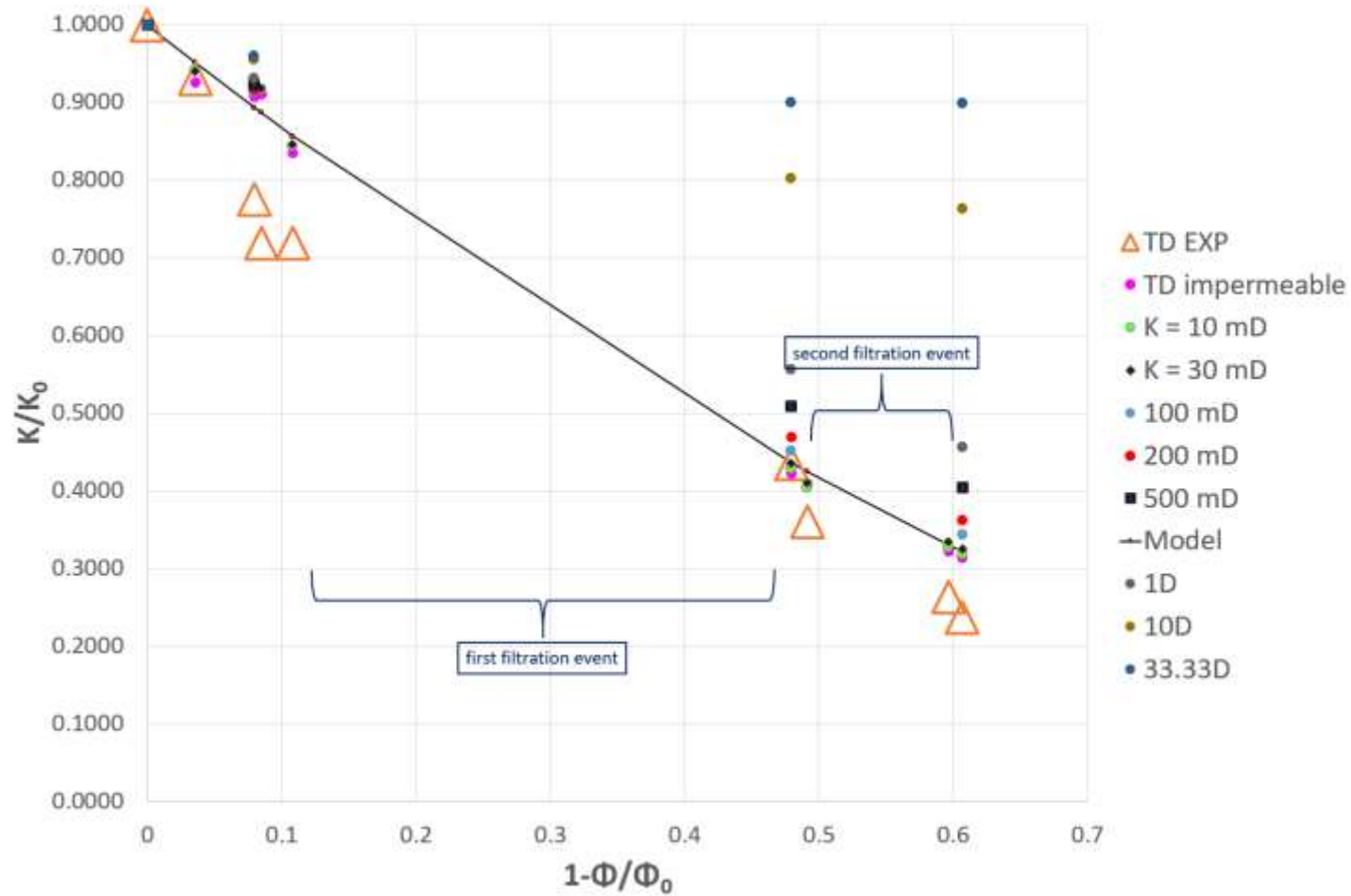


Figure 19: Comparison of experimental and simulation results of the TD. Normalized porosity-permeability reduction for two stages of flooding (BSF and NF). The experimentally obtained data shows a greater reduction in permeability, reasons may be the plugged flowlines and valves, which are not covered in the simulations, and were accompanied by filtration events

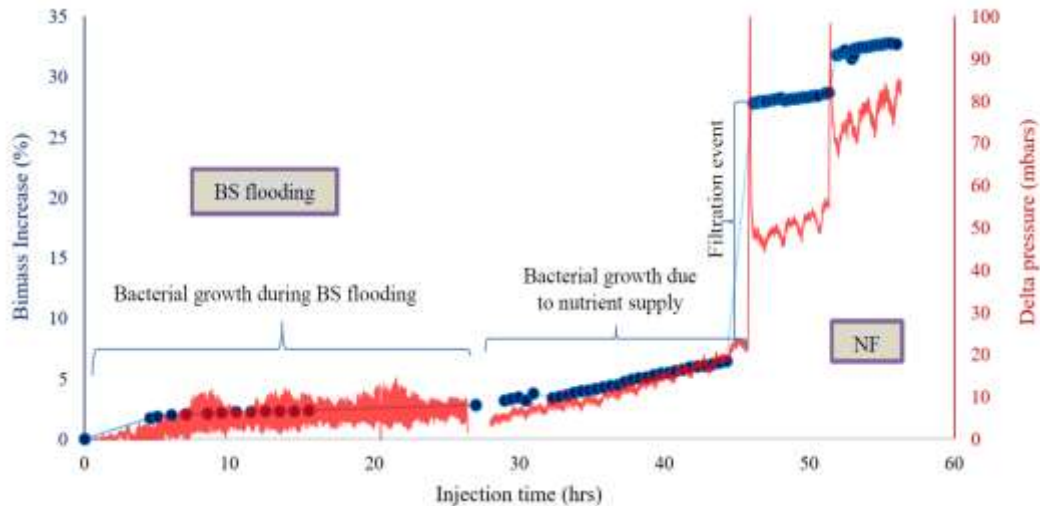


Figure 20: Correlation between the growth of biomass and pressure drop across the micromodel over the bacterial suspension flooding (BS flooding) and nutrient flooding (NF). The spikes correspond to filtration events, as indicated in the figure [adapted from (Hassannayebi, 2019)]

4.3 Velocity

To gain further knowledge and understanding about the behavior of the fluid in the pore space as well as within the biomass, the velocity field was analyzed. Therefore, a python/numpy script was coded to extract the velocity values at the zone of interest from the volume field generated within the framework of the numerical simulations. The implemented code is shown in detail in Appendix A. Furthermore, a macro, which was provided by Dr. Hinz (Math2Market GmbH), was utilized to evaluate the occurrence of velocities for different scenarios.

4.3.1 Influence of Permeable Biofilm on Velocity

The plot of the influence of permeable biofilm on velocity is shown in Figure 21. The ordinate counts the occurrence of the velocities marked on the axis of abscissa. Anyhow, the highest velocity values have been achieved by the impermeable case, which is in line with the expected results. Due to the fact, that the pore fluid cannot penetrate the accumulated biomass, the velocity must be higher compared to the permeable cases. Further, the case with an internal permeability of 100 mD must show higher velocities than the cases with 300 mD to 33.33 D. The less flow area is available to the fluid, the higher the velocity (see Figure 21). As the internal permeability of the biomass is increased, the moderate velocities on the right-hand side of the figure tend to increase.

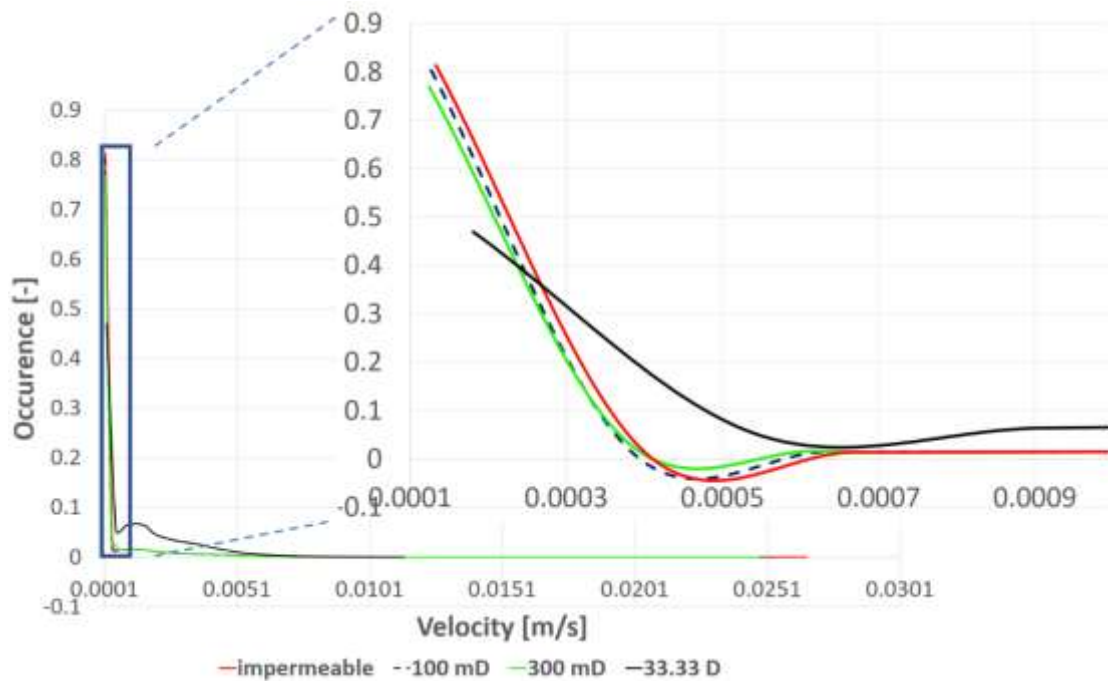
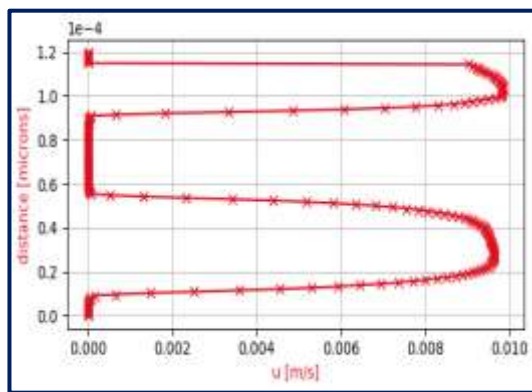
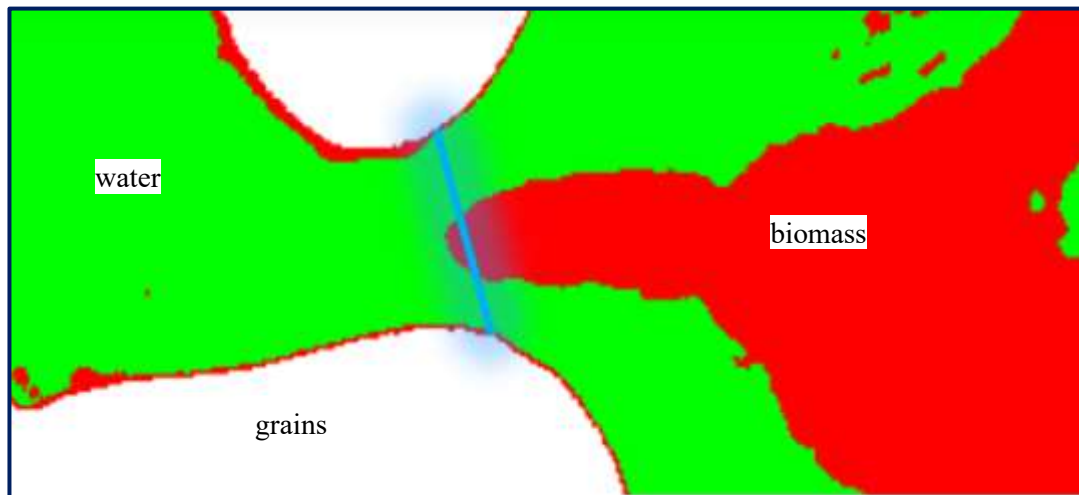


Figure 21: Velocity count plot of the TD for different internal permeability of the biomass. As expected, the impermeable case achieved the highest velocity values (red line).

To get further information about the influence of the permeable biofilm on the hydraulic properties of the pore network, the velocity of different permeability cases was compared at the same point within the structure. To gain knowledge about the influence of the internal permeability a location was chosen where a stream tracer accumulated between two grains to study the zone of transition from the pore space to the biomass and vice versa. The line where the plotted velocity values were taken from is indicated in Figure 22 with a blue line.

As expected, the velocity is zero for the impermeable case within the biomass. An increase in the permeability of the biomass is accompanied by an increase in the velocity values within the biomass. In contrast, the velocity in the pore space is decreasing as the fluid is not forced to bypass an obstacle. Furthermore, the change in velocity values at the grain-boundaries is remarkable; as the internal permeability of the biomass is raised, the velocities in the biofilm attached to the grain surface are increasing as well.

The plotted values are also in line with the velocity occurrence plot, where the highest velocity values were achieved with the highest permeability case (33.33 D).



Impermeable biomass

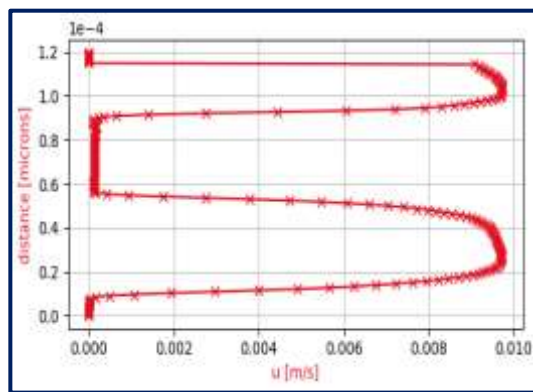
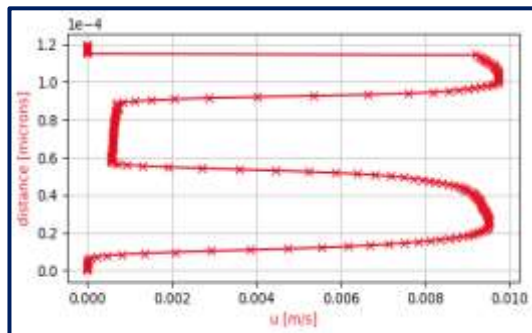
 $K_{\text{biomass}} = 10\text{mD}$  $K_{\text{biomass}} = 100\text{mD}$  $K_{\text{biomass}} = 33.33\text{D}$

Figure 22: Flow profile with different internal permeability of the biomass. The spot where the velocity values are taken from is shown on top, the blue line indicates the exact location. Conspicuously is the transition of the profile from the open pore space to the accumulated biomass and vice versa. In the impermeable case, the velocity is zero and is continuously increasing as the internal permeability is raised. This increase in velocity within the biomass is accompanied by a reduction in the overall velocity.

4.3.2 Analysis of Dimensionless Péclet Number – Advection versus Diffusion

To examine whether the fluid flow within the biomass is a result of diffusion or advection, the dimensionless Pe number was calculated for a set of different internal permeability of the biomass. As illustrated in the following figure, five spots were chosen to investigate the behavior of the fluid within the biomass with increased permeability. One stream tracer and four big cluster complement the chosen spots. The yellow line drawn in the selected clusters of accumulated biomass represents the area of readout of the velocity values. Anyhow, the results are shown in Figure 23. The blue lines in the diagram correspond to the diffusion constant (D), which was adopted from Pintelon et al. (2012), and a Pe number of one, whereas the purple lines correspond to a Pe number of ten, which was plotted based on the assumption of Bijeljic et al. (2004), who stated that Pe numbers in excess of ten indicate advection dominance.

As the permeability of the biomass is raised, the Pe number increases, by cause of the pore fluid can penetrate the biomass more easily. This is in line with the extracted velocity values in the figure above. The cluster C5 shows the least dominance of advection. It reaches a Pe number of one at about 62 mD, Pe number of 10 is achieved at 283 mD. The opposite is the case taking a look at the first three clusters (C2 to C4), where the Pe number of one is reached at an internal permeability of fewer than ten millidarcy (8.2 mD) and the advection dominated part ($Pe > 10$) is surpassed at 83 mD. The inspected clusters in the vicinity of the inlet and outlet (C1 and C5) may also differ in their behavior because they are smaller in length, which is in the calculation of the Pe number in the numerator, thus, higher values are promoting advection dominance.

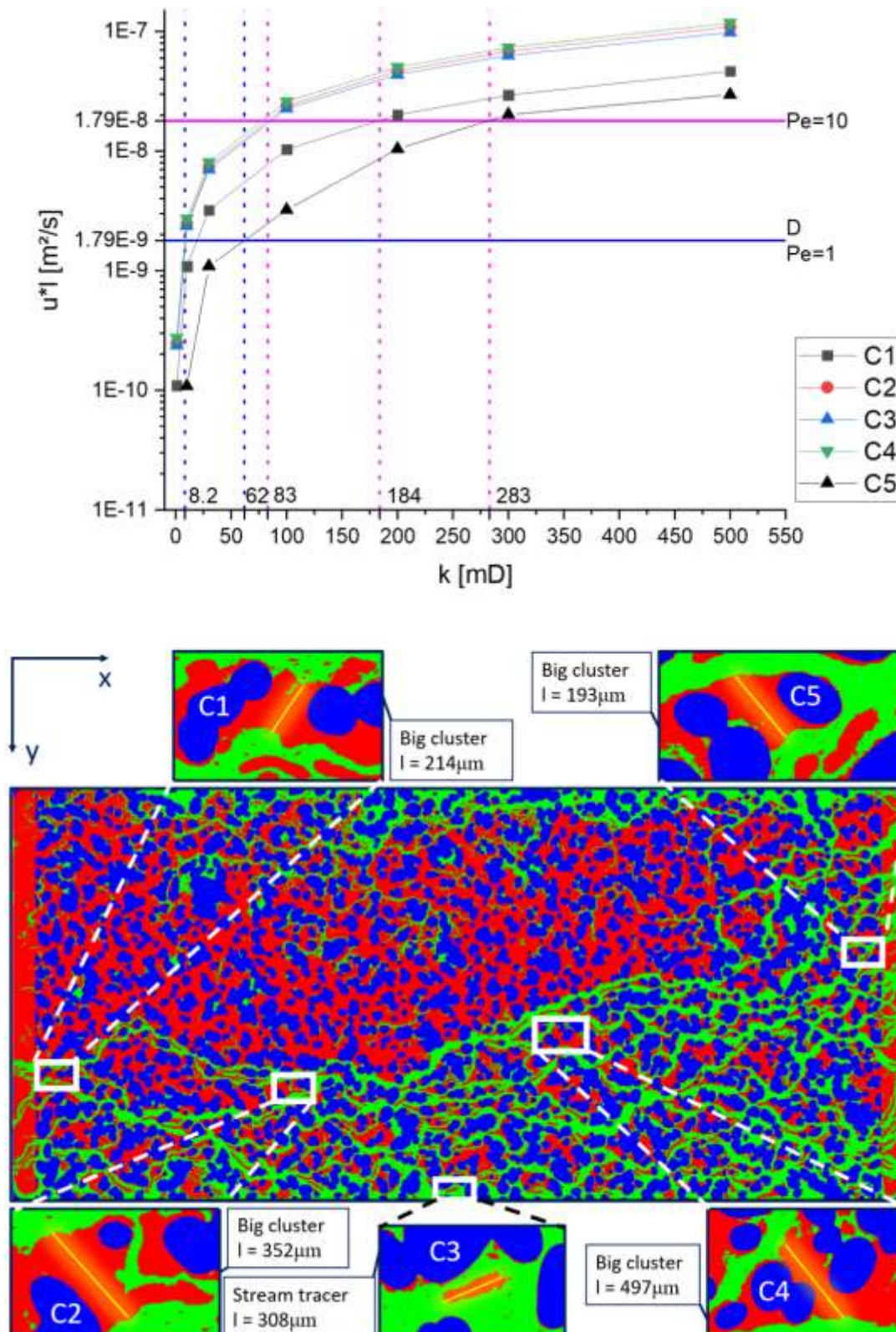


Figure 23: Comparison of the labelled clusters (lower image) at different internal permeability of the biomass (axis of the abscissa). On the ordinate the product of velocity (u) times characteristic length (l) (cluster length) is plotted. D is the diffusion constant, which was set to $1.79\text{e-}9$ m²/s. Based on literature, the transition to the dominance of advection is set to ten. The values must be treated with care, due to the tremendous influence of the characteristic length (l).

4.3.3 Velocity Distribution within the Permeable Biomass

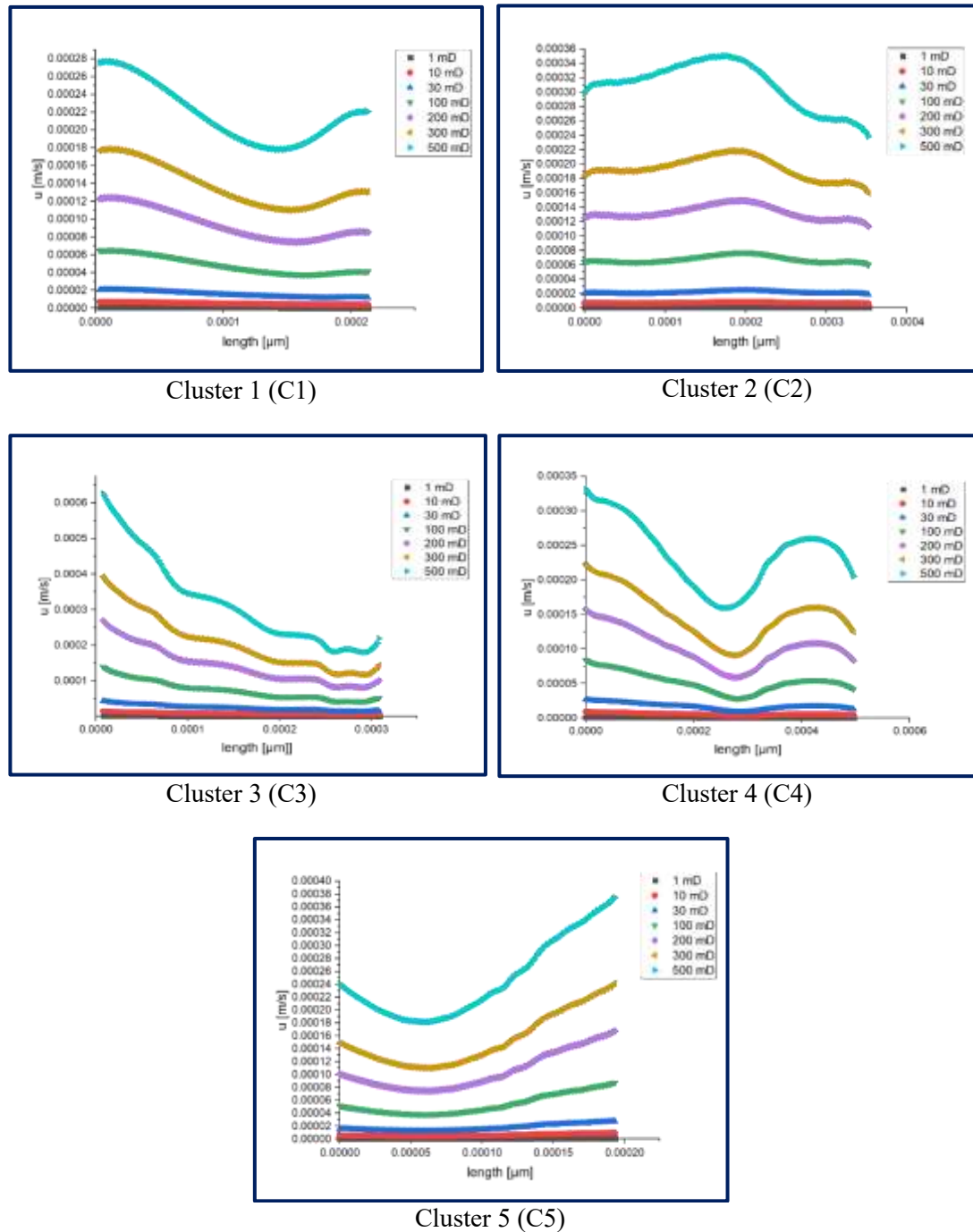


Figure 24: Velocity plot over penetration depth (biomass). Velocity at the boundary is a function of the velocity in the pore space and the angle of the accumulated biomass to the velocity vector. The shape of the curve stays always the same, optical variations are due to the lower values achieved with lower internal permeability of the biomass.

The figure above displays the velocities within the biomass versus the length. The shape of the curve at different permeability is identical, the different shapes in the plot arise from the vast differences in velocity. The exact location of the observed clusters is shown in Figure 23.

The resulting velocity values are not only a function of the internal permeability, but also the angle of the fluid-biomass interface. The highest values are achieved if the flow is perpendicular to the biomass, as it is the case in Cluster 3, which has accumulated as stream tracer (see Figure 24). Conspicuously is also the shape of the curve of Cluster 2, where the peak, thus, the highest velocity, occurs neither at the beginning, nor in the end, but in the middle. Taking a look at the cluster's location, the vicinity to a narrow pore channel, who is forcing the fluid to flow with higher velocity within this passage, is noticeable and explaining the high values observed in the middle of the cluster. A contrary result was delivered by Cluster 4. Again, looking at the exact location it is visible, that this cluster is embedded with grains, hindering the pore fluid to supply the biomass with nutrients perpendicular to flow direction. The same accounts for Cluster 5, which shows higher velocities at the bottom than on top of the cluster, again, a function of how the velocity vector is aligned to the fluid-biomass interface.

4.4 Discussion Section

The main focus of this thesis was to study whether the accumulated biomass has an internal porosity and permeability or not, and if so, what is the resulting impact on the hydraulic properties of the pore network. Therefore, the permeability porosity relationship was computed. To investigate this relationship simulations were conducted on both, the ROI and the TD. The results of the TD were compared to the experimentally obtained results.

Taking a look at Figure 19, it is noticeable that internal permeabilities below 100 mD cannot be distinguished from the impermeable case. In the studied scenario, the impact seems to be negligible. Again, taking the law of Hagen-Poiseuille into account, we would end up with a permeability of about 33.33 D, which is more than a factor of 300 compared to the 100 mD of internal permeability of the accumulated biomass. To sum it up, if the permeability of the observed systems is considerably larger than the internal permeability of the biomass, the biomass may be treated as impermeable.

The cases with the underlying assumption of constant in-biomass permeability can be described with a single power-law behavior. This does not hold anymore if the internal permeability of the biomass is scaled to the gray values and a variation is introduced. In this case, BSF and NF regimes show a distinct behavior.

Questionable is the structure of the biomass itself. If it is considered as a gel, the nutrient transport would be a result of pure diffusion and it may not be considered as a porous medium itself.

Furthermore, the results plotted in Figure 19 indicated, that the internal permeability of the biomass may not exceed 100 mD. As already mentioned, below 100 mD no distinction with the

naked eye is possible. The simulated data (impermeable case) correlated well with the experimental achieved data points. If the gap between the experimental and simulated data prior to the first filtration event and in the vicinity of the second filtration event is a result of the plugged flowlines and valves is a pending issue, since these plugged flowlines and valves were not included in the numerical simulations.

Figure 23 is indicating an advection dominance in the in-biomass nutrient transport at biomass permeability of 10 mD and above. The results are indicating that as we introduce a biomass permeability, the supply of nutrients within the biomass is a result of advection. Even Pe numbers in excess of ten were achieved with in-biomass permeability below 100 mD.

Noteworthy is also the velocity distribution within the studied clusters of accumulated biomass. Figure 24 indicates the relative importance of the angle and the velocity in which the pore fluid hits the biomass interface. The general importance of the velocity gets visible by examining the varying shapes of the accumulated biomass. If the biomass settles within a preferential flow pathway (high-velocity region) the biomass' shape equates stream tracers, which are promoting channelization, whereas low-velocity regions allow the formation of so-called clumps. In general, the biomass accumulates rather heterogeneous in the pore space. The resulting shape of the biomass aggregate is as well a function of viscous dissipation, the loss of energy from the pore fluid to the biomass. Figure 22 shows the consequence of the internal permeability of the biomass on the velocities. As the permeability is increased, the velocity in the pore space is decreasing.

Chapter 5

Summary, Conclusions, and Future Work

To study the impact of microbial growth on the hydraulic properties of subsurface gas storage sites and in-situ gas conversion, experimental images, which were achieved in the course of a doctoral thesis, were processed. This was the starting point of this thesis. As a consequent step, these images were thresholded to specify which gray values belong to the biomass, the pore space, and the pore fluid. The range of gray values belonging to the biomass was divided into six subgroups, to advise different values of internal permeability. As a next step, the images were layered to obtain a structure that equals the experimental setup and to conduct flow simulations. Pore-scale numerical simulations were conducted with both, varying and uniform permeability, on the ROI and the TD. The results were plotted to study the reduction in porosity and permeability over time. Further, the results obtained on the TD were compared to the ones experimentally achieved.

Moreover, the flow field was studied in detail. This is the second major topic and is related to mass transport as well as nutrient supply within the accumulated biomass. A python script was coded to extract the velocities values between two points of interest in space. Besides that, the velocity values were used to study the velocity distribution within the biomass and to evaluate the dimensionless Péclet number to investigate whether the nutrient supply in the accumulated biomass is a result of diffusion or advection. Hence, several clusters were analyzed scattered across the total domain. Moreover, the script was utilized to plot the velocities between two points of interest in space along a line to investigate the change in the flow profile as the internal permeability of the biomass is varied.

The main goal of this thesis was to study the impact of microbial growth on the hydraulic properties of the pore space. The major ambition was to study the presence of an internal permeability and porosity of the accumulated biomass. The results achieved with the numerical simulations were compared to the ones experimentally obtained. Some data points show an

excellent match, whereas the ones prior to the two major filtration events tend to deviate from the simulated data points. Reasons may be found in the plugged flowlines and valves which were observed in the experiments but were not implemented in the numerical simulations. The uniform permeability cases can be described by a single power-law function. This is not valid for the case with varying permeability where BSF and NF show a distinct behavior.

Besides that, the comparison of the simulation results on the TD exhibit, that a distinction of data points generated with an internal permeability of 100 mD and below to the impermeable case is not possible with the naked eye. Hence, the impact on the hydraulic properties of the pore space may be a function of the intrinsic permeability. In the studied case this impact seems to be negligible since the permeability of the system is considerably larger compared to the internal permeability of the biomass. In other words, the impact on the hydraulic properties may increase as the overall permeability of the observed system decreases. Following the law of Hagen-Poiseuille, calculating the permeability with the extension in the z-direction (20 μm), the resulting permeability of the open pore space is about 33.33 D. Again, due to the high contrast of the system permeability and the internal permeability of the accumulated biomass, which may be as high as 100 mD, the impact seems to be negligible.

Anyhow, biomass growth was observed in dead-end areas, whereat the supply of nutrients must happen through the biomass itself. Studying the in-biomass nutrient supply, results are indicating that even small internal permeabilities (10 mD and above), which are not affecting the hydraulic properties of the pore space, may lead to an advection dominance in the nutrient supply of the biomass. Anyhow, the results obtained must be

Furthermore, the results obtained via studying the velocity distribution within the biomass indicate the importance of the angle the pore fluid is hitting the interface of the biomass aggregates, as well as the proximity to a high-velocity channel.

Via an examination of the varying shapes of the biomass, the significance of the velocity is getting once more visible. Aggregates, which accumulate within a preferential flow pathway of the pore fluid are likely to form stream tracers, which are promoting channelization, whereas biomass in low-velocity regions tends to settle as bigger aggregates, so-called clumps. In general, the biomass accumulates rather heterogeneously in the pore space, in such a way that the TD may not necessarily correspond to a representative elementary volume (REV). Furthermore, the resulting shape of the accumulated biomass is as well a result of viscous dissipation since the pore fluid is losing energy to the biomass.

5.1 Future Work

It would be of paramount interest to measure the nutrient concentration at the inlet as well as at the outlet to gain deeper knowledge about the nutrient consumption within the micromodel. Furthermore, the different time stages could be compared with the dimensionless Damköhler numbers.

Furthermore, the exact mechanisms of nutrient supply within the biomass require further attention. Therefore, also the detailed structure of the biomass itself needs further attention. Considering the structure of the biomass as a gel, the transport of nutrients would be a result of pure diffusion. Thus, the biomass may not have an internal permeability and no micro-porosity.

Additionally, several inaccessible zones for biomass accumulation and particle transport were recognized within the pore space. Hence, it would be of interest to correlate the location of biomass settlement with the flow field.

Due to the rather inhomogeneous accumulation of biomass within the pore space, the TD may not correspond to a REV, hence simulations on an additional ROI may be of interest.

Moreover, the selection of the critical length in the calculation of the Pe number is critical. In this study, the labeled length in the x-y plane was chosen since the variation in length was minor. To get comparable results, the selection of the critical length needs further attention.

Based on these results, additional cases of varying internal permeability with values of 100 mD and below would be of interest.

Chapter 6

References

- Ahmad, I. and Husain, F. M. (2017) *Biofilms in plant and soil health*. John Wiley & Sons.
- Bijeljic, B., Muggeridge, A. H. and Blunt, M. J. (2004) 'Pore-scale modeling of longitudinal dispersion', *Water Resources Research*. John Wiley & Sons, Ltd, 40(11). doi: 10.1029/2004WR003567.
- Carrel, M. *et al.* (2018) 'Pore-Scale Hydrodynamics in a Progressively Bioclogged Three-Dimensional Porous Medium: 3-D Particle Tracking Experiments and Stochastic Transport Modeling', *Water Resources Research*. John Wiley & Sons, Ltd, 54(3), pp. 2183–2198. doi: 10.1002/2017WR021726.
- D'Humières, D. *et al.* (2002) 'Multiple-Relaxation-Time Lattice Boltzmann Models in Three Dimensions', *Philosophical transactions. Series A, Mathematical, physical, and engineering sciences*, 360, pp. 437–451. doi: 10.1098/rsta.2001.0955.
- Donlan, R. (2002) 'Biofilms: Microbial Life on Surfaces', *Emerging infectious diseases*, 8, pp. 881–890. doi: 10.3201/eid0809.020063.
- Flemming, H.-C., Szewzyk, U. and Griebe, T. (2000) *Biofilms: investigative methods and applications*. CRC Press.
- Gabrielli, P. *et al.* (2020) 'Seasonal energy storage for zero-emissions multi-energy systems via underground hydrogen storage', *Renewable and Sustainable Energy Reviews*, 121, p. 109629. doi: <https://doi.org/10.1016/j.rser.2019.109629>.
- Gerlach, R. and Cunningham, A. (2010) 'Influence of Biofilms on Porous Media Hydrodynamics. In: Porous Media: Applications in Biological Systems and Biotechnology. s.l.:Taylor and Francis Group, LLC, pp. 174-230', in, pp. 173–230. doi: 10.1201/9781420065428-6.

- Götz, M. *et al.* (2016) 'Renewable Power-to-Gas: A technological and economic review', *Renewable energy*, 85, pp. 1371–1390. doi: 10.1016/j.renene.2015.07.066.
- Harvey, R. W. and Garabedian, S. P. (1991) 'Use of colloid filtration theory in modeling movement of bacteria through a contaminated sandy aquifer', *Environmental Science & Technology*. American Chemical Society, 25(1), pp. 178–185. doi: 10.1021/es00013a021.
- Hassannayebi, N. (2019) *An assessment of underground hydrogen storage: Transport, geochemistry, and bioactivity*.
- Hilden, J., Linden, S. and Planas, B. (2020) 'Flow Dict User Guide GeoDict Release 2020'.
- Hinz, C. (2020) *Reactive flow in porous media based on numerical simulations at the pore scale*. Johannes Gutenberg-Universität, Institut für Geowissenschaften: Univ. Available at: <http://nbn-resolving.org/urn:nbn:de:hebis:77-diss-1000034554>.
- Hommel, J., Coltman, E. and Class, H. (2018) 'Porosity–Permeability Relations for Evolving Pore Space: A Review with a Focus on (Bio-)geochemically Altered Porous Media', *Transport in Porous Media*. Springer Netherlands, pp. 589–629. doi: 10.1007/s11242-018-1086-2.
- Jeong, H. Y. *et al.* (2018) 'A review on clogging mechanisms and managements in aquifer storage and recovery (ASR) applications', *Geosciences Journal*, 22(4), pp. 667–679. doi: 10.1007/s12303-017-0073-x.
- Landa Marbán, D. *et al.* (2018) 'A Pore-Scale Model for Permeable Biofilm: Numerical Simulations and Laboratory Experiments', *Transport in Porous Media*, 127. doi: 10.1007/s11242-018-1218-8.
- Lappin-Scott, H. M., Cusack, F. and Costerton, J. W. (1988) 'Nutrient resuscitation and growth of starved cells in sandstone cores: a novel approach to enhanced oil recovery.', *Applied and environmental microbiology*, 54(6), pp. 1373–1382.
- Linden, S., Hagen, H. and Wiegmann, A. (2014) *The LIR Space Partitioning System Applied to Cartesian Grids*. doi: 10.1007/978-3-642-54382-1_19.
- Martin, R. (2013) *Clogging Issues Associated with Managed Aquifer Recharge Methods*. Australia: IAH Commission on Managing Aquifer Recharge.
- Martin, R. E., Bouwer, E. J. and Hanna, L. M. (1992) 'Application of clean-bed filtration theory to bacterial deposition in porous media', *Environmental Science & Technology*. American Chemical Society, 26(5), pp. 1053–1058. doi: 10.1021/es00029a028.
- Ott, H. *et al.* (2014) 'Microscale solute transport and precipitation in complex rock during drying', *Geophysical Research Letters*. John Wiley & Sons, Ltd, 41(23), pp. 8369–8376. doi:

10.1002/2014GL062266.

Pintelon, T. R. R. *et al.* (2012) 'The effect of biofilm permeability on bio-clogging of porous media', *Biotechnology and bioengineering*. Wiley Online Library, 109(4), pp. 1031–1042.

Thullner, M. and Baveye, P. (2008) 'Computational pore network modeling of the influence of biofilm permeability on bioclogging in porous media', *Biotechnology and Bioengineering*. Wiley Online Library, 99(6), pp. 1337–1351.

Tufenkji, N. (2007) 'Modeling microbial transport in porous media: Traditional approaches and recent developments', *Advances in Water Resources*, 30, pp. 1455–1469.

Warsi, O. M. and Dykhuizen, D. E. (2017) 'Evolutionary implications of Liebig's law of the minimum: Selection under low concentrations of two nonsubstitutable nutrients.', *Ecology and evolution*, 7(14), pp. 5296–5309. doi: 10.1002/ece3.3096.

Willey, J. M. *et al.* (2008) *Prescott, Harley, and Klein's Microbiology*. McGraw-Hill Higher Education (McGraw-Hill Higher Education). Available at: <https://books.google.at/books?id=qJVwQgAACAAJ>.

Yao, K.-M., Habibian, M. T. and O'Melia, C. R. (1971) 'Water and waste water filtration. Concepts and applications', *Environmental Science & Technology*. American Chemical Society, 5(11), pp. 1105–1112. doi: 10.1021/es60058a005.

Zhang, P. *et al.* (2001) 'Extended tailing of bacteria following breakthrough at the Narrow Channel Focus Area, Oyster, Virginia', *Water Resources Research*. John Wiley & Sons, Ltd, 37(11), pp. 2687–2698. doi: 10.1029/2000WR000151.

Appendix A

Python Script – Velocity Plot

A python script was written to extract and plot the calculated velocities between two points of interest in space. The code was written with GeoPython, which is the GeoDict– Python interface, implemented in GeoDict©.

A.1 Script

```
import numpy as np

import matplotlib.pyplot as plt

import scipy.ndimage

import math

Header = {

    'Release'      : '2020',

    'Revision'     : '15936',

}

Description = "Create a velocity profile plot.

(c) 2020 Boris Jammerneegg"

Variables = {

    'NumberOfVariables' : 9,

    'Variable1' : {
```

```
'Name'      : 'nx',
'Label'     : 'x-dimension (structure)',
'Type'      : 'int',
'ToolTip'   : 'Number of voxels in x-direction',
'BuiltinDefault' : '11535',
},
'Variable2' : {
'Name'      : 'ny',
'Label'     : 'y-dimension (structure)',
'Type'      : 'int',
'ToolTip'   : 'Number of voxels in y-direction',
'BuiltinDefault' : '5500',
},
'Variable3' : {
'Name'      : 'nz',
'Label'     : 'z-dimension (structure)',
'Type'      : 'int',
'ToolTip'   : 'Number of voxels in z-direction',
'BuiltinDefault' : '5',
},
'Variable4' : {
'Name'      : 'x',
'Label'     : 'x-coordinate Point #1',
'Type'      : 'int',
'ToolTip'   : 'ROI',
'BuiltinDefault' : '1',
},
'Variable5' : {
```

```
'Name'      : 'x1',
'Label'     : 'x-coordinate Point #2',
'Type'      : 'int',
'ToolTip'   : 'ROI',
'BuiltinDefault' : '1',
},
'Variable6' : {
  'Name'     : 'y',
  'Label'    : 'y-coordinate Point #1',
  'Type'     : 'int',
  'ToolTip'  : 'ROI',
  'BuiltinDefault' : '1',
},
'Variable7' : {
  'Name'     : 'y1',
  'Label'    : 'y-coordinate Point #2',
  'Type'     : 'int',
  'ToolTip'  : 'ROI',
  'BuiltinDefault' : '1',
},
'Variable8' : {
  'Name'     : 'z',
  'Label'    : 'z-coordinate Point #1',
  'Type'     : 'int',
  'ToolTip'  : 'ROI',
  'BuiltinDefault' : '1',
},
'Variable9' : {
```

```
'Name'      : 'z1',  
'Label'     : 'z-coordinate Point #2',  
'Type'      : 'int',  
'ToolTip'   : 'ROI',  
'BuiltinDefault' : '1',  
}}
```

```
vel = gd.getVolumeField('Velocity')
```

```
num = 200
```

```
if x == x1 and z == z1:
```

```
    a = vel[x, y:y1, z]
```

```
    a_max = np.amax(a)
```

```
    b = a/a_max
```

```
    k = b.tolist()
```

```
    w = len(k)
```

```
    m = (y1-y)*1.892e-6
```

```
    n=np.linspace(0, m, w)
```

```
    d_max = np.amax(n)
```

```
    d_rel = n/d_max
```

```
    q = d_rel.tolist()
```

```
elif y == y1 and z == z1:
```

```
    ...
```

```
elif x == x1 and y == y1:
```

```
    ...
```

```
elif z == z1 and x1 > x and y1 > y:
```

```
    u_field = vel[x:x1, y:y1, z]
```

```
    u_abs = np.absolute(u_field)
```

```
    x0, y0 = 0, 0
```

```
x2, y2 = x1-x, y1-y
d, e = np.linspace(x0, x2, num), np.linspace(y0, y2, num)
zi = scipy.ndimage.map_coordinates(u_abs, np.vstack((d,e)))
u = np.absolute(zi)
u_max = np.amax(u)
u_rel = u/u_max
k = u_rel.tolist()
m = math.sqrt((y1-y)**2 + (x1-x)**2)*1.892e-6
n=np.linspace(0, m, num)
o = np.absolute(n)
d_max = np.amax(o)
d_rel = o/d_max
q = d_rel.tolist()

elif z == z1 and x1 > x and y > y1:
    ...

elif z < z1 and x < x1 and y < y1:
    u_field = np.absolute(vel[x:x1, y:y1, z:z1])
    u_abs = np.absolute(u_field)
    x0, y0, z0 = 0, 0, 0
    x2, y2, z2 = (x1-x), (y1-y), (z1-z)
    d, e, f = np.linspace(x0, x2, num), np.linspace(y0, y2, num), np.linspace(z0, z2, num)
    zi = scipy.ndimage.map_coordinates(u_abs, np.vstack((d,e,f)))
    u = np.absolute(zi)
    u_max = np.amax(u)
    u_rel = u/u_max
    k = u_rel.tolist()
```

```
m = math.sqrt((x1-x)**2 + (y1-y)**2 + (z1-z)**2)*1.892e-6
n=np.linspace(0, m, num)
o = np.absolute(n)
d_max = np.amax(o)
d_rel = o/d_max
q = d_rel.tolist()

elif z > z1 and x < x1 and y < y1:
    ...
elif z < z1 and x < x1 and y > y1:
    ...
elif z > z1 and x < x1 and y > y1:
    ...
elif x > x1 and z < z1 and y < y1:
    ...
elif x > x1 and z > z1 and y > y1:
    ...
elif x > x1 and z > z1 and y < y1:
    ...
elif x > x1 and z < z1 and y > y1:
    ...

gDlg = gd.makeGraphDialog()
graph1 = gDlg.addGraph("Velocity profile", "u/u_max", "d/d_max")
graph1.addData(k, q, "vel profile")
gDlg.run()
```